

Mo(Al Si_{1-x})₂ healing particles for high temperature ceramics and encapsulation by selective oxidation of aluminium

Ding, Zhaoying; Brouwer, Johannes C.; Kwakernaak, Cees; Zhu, Jia Ning; Popovich, Vera; Hermans, Marcel J.M.; Sloof, Willem G.

DOI

[10.1016/j.matdes.2022.111577](https://doi.org/10.1016/j.matdes.2022.111577)

Publication date

2023

Document Version

Final published version

Published in

Materials and Design

Citation (APA)

Ding, Z., Brouwer, J. C., Kwakernaak, C., Zhu, J. N., Popovich, V., Hermans, M. J. M., & Sloof, W. G. (2023). Mo(Al Si_{1-x})₂ healing particles for high temperature ceramics and encapsulation by selective oxidation of aluminium. *Materials and Design*, 225, Article 111577. <https://doi.org/10.1016/j.matdes.2022.111577>

Important note

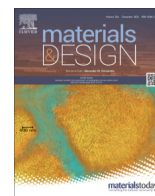
To cite this publication, please use the final published version (if applicable). Please check the document version above.

Copyright

Other than for strictly personal use, it is not permitted to download, forward or distribute the text or part of it, without the consent of the author(s) and/or copyright holder(s), unless the work is under an open content license such as Creative Commons.

Takedown policy

Please contact us and provide details if you believe this document breaches copyrights. We will remove access to the work immediately and investigate your claim.



Mo(Al_xSi_{1-x})₂ healing particles for high temperature ceramics and encapsulation by selective oxidation of aluminium



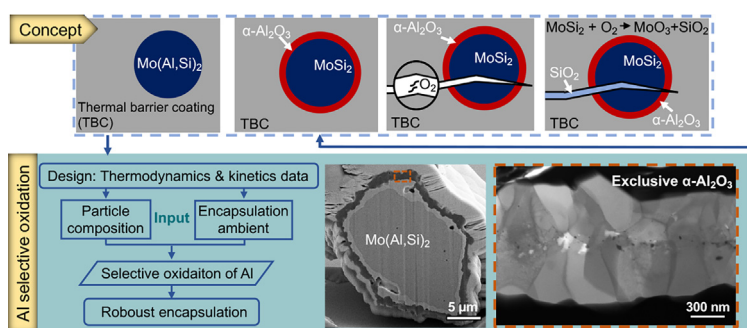
Zhaoying Ding, Johannes C. Brouwer, Cees Kwakernaak, Jia-Ning Zhu, Vera Popovich, Marcel J.M. Hermans, Willem G. Sloof*

Department of Materials Science and Engineering, Delft University of Technology, Mekelweg 2, 2628 CD Delft, the Netherlands

HIGHLIGHTS

- Healing particles of Mo(Al_xSi_{1-x})₂ is designed for encapsulation in terms of alumina shell thickness, particle size and fraction Al dissolved.
- By replacing Si by Al in MoSi₂, a strong crack damage healing ability is maintained (relative volume expansion $\geq 40\%$).
- By oxidation in a low pO_2 ambient, volatile Mo-oxide formation was inhibited and exclusive formation of α -Al₂O₃ shell was promoted.
- A dense α -Al₂O₃ shell with thickness of 1.3 μm envelops the MoSi₂ healing particles was achieved.
- The encapsulation method designed provides MoSi₂ particles with 86 % less weight loss upon oxidation preserving the healing capacity.

GRAPHICAL ABSTRACT



ARTICLE INFO

Article history:

Received 7 October 2022

Revised 27 December 2022

Accepted 30 December 2022

Available online 31 December 2022

Keywords:

Encapsulation

Mo(Al,Si)₂

Alumina scale growth

Oxidation

Self-healing thermal barrier coatings

ABSTRACT

To prevent premature triggering of the healing reaction in Mo-Si containing self-healing thermal barrier coating system, an oxygen impenetrable shell (α -Al₂O₃) around the sacrificial healing particles (MoSi₂) is desired. Here an encapsulation method is presented through selective oxidation of Al in Mo(Al_xSi_{1-x})₂ particles. Healing particles of Mo(Al_xSi_{1-x})₂ is designed in terms of alumina shell thickness, particle size and fraction Al dissolved. By replacing Si by Al in MoSi₂ up to the maximum solubility ($x = 0.65$) a strong crack healing ability is maintained (relative volume expansion $\geq 40\%$). The formed exclusive α -Al₂O₃, featuring a two-layered structure, results from a counter-diffusion process along the grain boundaries, and its oxidation kinetics fits well with the 3D diffusion-Jander model. After 16 h exposure in gaseous ambient with a pO_2 of 5×10^{-10} atm. at 1100 °C, a closed and dense shell of α -Al₂O₃ is formed with a thickness of about 1.3 μm . The oxide shell produced under this condition provided healing particles with significantly improved stability upon exposure to high pO_2 of 0.2 atm. at 1100 °C for 50 h. The particles after exposure feature an inner core of MoSi₂ with Al completely consumed and an oxide shell of α -Al₂O₃.

© 2023 The Authors. Published by Elsevier Ltd. This is an open access article under the CC BY license (<http://creativecommons.org/licenses/by/4.0/>).

* Corresponding author.

E-mail address: w.g.sloof@tudelft.nl (W.G. Sloof).

1. Introduction

Thermal barrier coating (TBC) systems are applied on the metallic components to provide thermal insulation from the hot gas stream in gas-turbine and jet engines [1–5]. With the use of a TBC, the modern gas-turbine engines are enabled to operate at gas temperatures well above the melting temperature of the nickel- or cobalt-based structural superalloys (~ 1300 °C), thereby improving engine efficiency and performance [1–5]. Yttria Partially Stabilized Zirconia (YPSZ) is the most widely used ceramic for TBCs because of its low thermal conductivity at high temperatures ($2.3 \text{ W}\cdot\text{m}^{-1}\cdot\text{°C}^{-1}$ at 1000 °C) in conjunction with high “strain tolerance” and chemical stability [1–5]. However, high stresses (2–6 GPa) are generated in these coatings when applied in e.g. gas turbine and jet engines where they are exposed to thermal cycles between operating and room temperature [1,4]. These stresses arise due to the difference in thermal expansion coefficients (CTEs) of the ceramic coating of YPSZ ($11\text{--}13 \times 10^{-6} \text{ °C}^{-1}$) and the metal substrate ($18\text{--}20 \times 10^{-6} \text{ °C}^{-1}$) [5] and give rise to the formation of microcracks, which propagate and eventually coalesce, and ultimately leading to TBC spallation [1,2,4–10]. The $\text{Mo}(\text{Al}_x\text{Si}_{1-x})_2$ particles are envisioned to be embedded in the bottom part of the TBC [7,11] near the interface with the bond coating where delamination cracks usually initiate [12,13].

A new self-healing TBC system was proposed to extend the lifetime [8,9,11,14] and has been applied successfully in a real TBC system [7,15,16] based on the oxidation of boron doped molybdenum disilicide ($\text{MoSi}_2\text{-B}$) particles embedded in ZrO_2 -based TBC [4,7,15]. When intercepted by cracks [8,9], the MoSi_2 healing particles oxidize preferentially and lead to the formation of amorphous SiO_2 , which fills the crack gap and establishes direct contact with the crack faces [4]. The amorphous SiO_2 subsequently reacts with the ZrO_2 of the matrix to form a load-bearing ZrSiO_4 phase, whereby wetting of the crack faces is achieved [4,17]. This prospective self-healing concept can be exploited to other high temperature structural ceramics as well [18,19].

The concept of self-healing TBC involves creating an inert and oxygen impenetrable shell around the sacrificial healing particle (MoSi_2), which prevents premature triggering of the healing reaction [7,15]. A shell composed of $\alpha\text{-Al}_2\text{O}_3$ is the most promising, since this oxide is stable at high temperatures in an oxidizing environment and exhibit a very low permeability of oxygen compared to other oxides [20–22]. The encapsulation of MoSi_2 particles with $\alpha\text{-Al}_2\text{O}_3$ has been realized by a precipitation [23] and a sol–gel [24] method followed by a calcining process. Both these encapsulation methods are applicable prior to embedding the healing particles into the YPSZ matrix as for example when manufacturing a self-healing TBC by spark plasma sintering [15].

Here an alternative method, based on selective oxidation [25,26] of Al in $\text{Mo}(\text{Al}_x\text{Si}_{1-x})_2$, is explored to encapsulate the MoSi_2 sacrificial particles for self-healing TBCs. This method has already been applied successfully when manufacturing a self-healing TBC by plasma spraying [7,16]. The advantage of this encapsulation by selective oxidation of Al in $\text{Mo}(\text{Al}_x\text{Si}_{1-x})_2$ is that the alumina shell on the healing particle is directly formed at temperatures comparable to those during high temperature operation of TBCs [1]. When the $\text{Mo}(\text{Al}_x\text{Si}_{1-x})_2$, healing particles are embedded in YPSZ, the encapsulation can be performed *in-situ* by annealing the system in an appropriate ambient before applied in working conditions, since the YPSZ matrix is permeable for oxygen [17]. Moreover, TBCs usually are porous [1–5].

In this work, for the encapsulation of $\text{Mo}(\text{Al}_x\text{Si}_{1-x})_2$, healing particles is designed in terms of alumina shell thickness, particle size and fraction Al dissolved. The conditions for the selective oxidation of Al to form a dense $\alpha\text{-Al}_2\text{O}_3$ shell such as temperature and oxygen

partial pressure are determined based on thermodynamic and kinetic data.

2. Theory and experimental procedures

2.1. Selective oxidation of Al in $\text{Mo}(\text{Al}_x\text{Si}_{1-x})_2$ particles

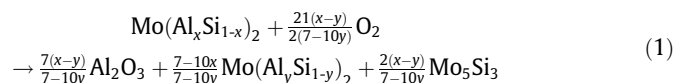
2.1.1. Composition and crystal structure

$\text{Mo}(\text{Al},\text{Si})_2$ appears with three different crystal lattice structures depending on the ratio of Al to Si ratio, which include: tetragonal (C11b), hexagonal (C40) and orthorhombic (C54) structures; see the Mo–Al–Si ternary phase diagram at 1500 °C in Fig. 1a. MoSi_2 exhibits the tetragonal (C11b) crystal structure, which has a small solubility of Al (1.9 at.% at 1500 °C). Further substitution of Si with Al results in $\text{Mo}(\text{Al},\text{Si})_2$ with a hexagonal (C40) crystal lattice structure, which exists over a wide composition range (up to about 30 at.% Al at 1500 °C). Beyond this composition, $\text{Mo}(\text{Al},\text{Si})_2$ takes the orthorhombic (C54) crystal lattice structure.

2.1.2. Oxidation

The temperature of 1100 °C at which the oxidation experiments are executed, is chosen in view of the application in thermal barrier coating systems [1,27,28]. In order to define the conditions for selective oxidation of Al of $\text{Mo}(\text{Al},\text{Si})_2$ at 1100 °C, the stability of the constituting elements and their oxides as a function of the oxygen partial pressure in a gaseous ambient is considered; see Fig. 2. The oxygen partial pressure (p_{O_2}) of 10^{-14} atm. lies just below the dissociation oxygen partial pressure of Mo-oxides at 1100 °C, but far above the dissociation oxygen partial pressure of Si- and Al-oxides according to the metal/oxide stability diagrams; see Fig. 2a–d. $\text{SiO}(\text{g})$ exist as the highest vapor pressure of about 10^{-10} atm. with a p_{O_2} of 10^{-14} atm. in the gaseous ambient; see Fig. 2d. During oxidation of $\text{Mo}(\text{Al},\text{Si})_2$ at 1100 °C with a p_{O_2} of 10^{-14} atm., the solid oxide of MoO_2 cannot be formed and the vapour pressures of the volatile Mo-oxides are very low ($<10^{-10}$ atm.). While the p_{O_2} of 5×10^{-10} atm. lies above the dissociation oxygen partial pressure of solid MoO_2 with the highest vapor pressure of gaseous $(\text{MoO}_3)_2$ is only about 10^{-6} atm. at 1100 °C. However, once the surface of the alloy is covered with a close layer of either silica or alumina, volatile Mo-oxides will likely cease to form. Since the dissociation oxygen partial pressure of Al_2O_3 is much lower than that of SiO_2 (10^{-31} atm. versus 10^{-25} atm., see Fig. 2b and 2c), alumina will be formed preferentially.

The selective oxidation of Al in $\text{Mo}(\text{Al},\text{Si})_2$, proceeds according to the following chemical reaction under a low p_{O_2} of 10^{-14} atm. at 1100 °C [29]:



where $\text{Mo}(\text{Al}_y\text{Si}_{1-y})_2$ is the intermediate product with $y \leq x$. The Al depletion path according to this reaction (Eq. (1)) is identified in the Mo–Si–Al phase diagram at 1100 °C; see Fig. 1b.

2.1.3. Kinetics

The kinetics of selective oxidation of the $\text{Mo}(\text{Al}_x\text{Si}_{1-x})_2$ is described in terms of its conversion according to Eq. (1) expressed as:

$$\alpha = \frac{m_t - m_0}{m_\infty - m_0} \Rightarrow \alpha = \frac{\Delta m / m_0}{(m_\infty / m_0) - 1} \quad (2)$$

where α is the converted fraction as a function of time, m_0 denotes the initial mass, m_t is the mass at time t , and m is the mass after full conversion.

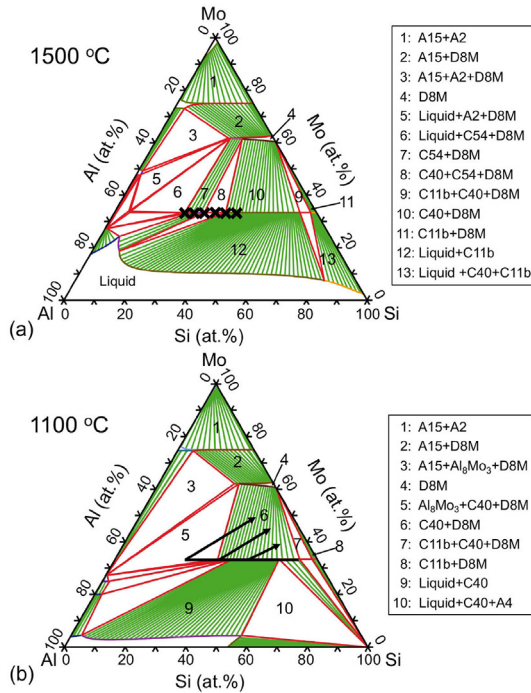
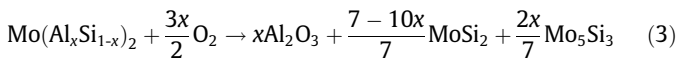


Fig. 1. Mo–Al–Si ternary phase diagram at (a) 1500 °C and (b) 1100 °C as calculated with Thermo-Calc software. The composition of the prepared alloys is indicated with crosses in (a) and the Al depletion paths upon oxidation are identified with arrows in (b). The C11b, C40 and C54 represent $\text{Mo}(\text{Al}_x\text{Si}_{1-x})_2$ having a tetragonal, hexagonal and orthorhombic crystal lattice, respectively. D8M is $\text{Mo}_5(\text{Al}_x\text{Si}_{1-x})_3$ with a tetragonal crystal lattice. A15 is $\text{Mo}_3(\text{Al}_x\text{Si}_{1-x})$ with a cubic crystal system, A2 is AlMo with a body-centered cubic crystal lattice, and A4 is Si with diamond crystal structure.

When all Al is consumed (i.e., $y = 0$), then according to Eq. (1) it holds that:



Hence:

$$m_\infty/m_0 = \frac{(\frac{7-10x}{7}M_{\text{MoSi}_2} + xM_{\text{Al}_2\text{O}_3} + \frac{2x}{7}M_{\text{Mo}_5\text{Si}_3})}{M_{\text{Mo}(\text{Al}_x\text{Si}_{1-x})_2}} \quad (4)$$

where M is the corresponding molar mass.

The rate of conversion into oxides upon thermal oxidation of the solid particles can be described with [30]:

$$\frac{d\alpha}{dt} = Ae^{-\frac{E_a}{RT}}f(\alpha) \quad (5)$$

where, A is the pre-exponential factor of the Arrhenius relation, E_a is the activation energy (J/mol), T is the absolute temperature (K), R is the gas constant, $f(\alpha)$ represents the reaction model, and α is the fraction converted, which is derived from gravimetric measurements; see Eqs (2) and (4). Separating variables and integrating Eq. (5) gives the integral form of the isothermal rate law [30]:

$$g(\alpha) = kt \quad (6)$$

$$\text{where } g(\alpha) = \int_0^\alpha \frac{d(\alpha)}{f(\alpha)} \quad (7)$$

$$\text{and } k = Ae^{-\frac{E_a}{RT}} \quad (8)$$

in which $g(\alpha)$ is the integral reaction model and k being the rate constant. An experimental value for the rate constant k at different temperatures can be obtained from plotting $g(\alpha)$ versus t .

The appropriate reaction model can be ascertained by plotting the experimentally determined converted fraction α as a function of a reduced time variable t/t_x , where t_x is the time required to reach a specified conversion (e.g., $\alpha = 0.25$); the so-called reduced-time plot [30,31]. Next, the experimental data are compared with theoretical reaction models [30], viz.: diffusion (D), Avrami-Erofeyev (A), order-based (F) or geometrical contraction (R) reaction models; see Supplementary material 1.1 for the solid-state kinetic models and their integral expressions. The reaction model that resembles the experimental data best is selected.

2.2. Experimental procedures

2.2.1. Synthesis of Mo–Si–Al alloys

Single phase $\text{Mo}(\text{Al}_x\text{Si}_{1-x})_2$ alloys were prepared by a one-step sintering process. Elemental powder of molybdenum (2–5 μm 99.95% purity, Chempur, Germany), silicon (45 μm 99.99% purity, TLS Technik GmbH, Germany) and aluminium (45 μm 99.8% purity, TLS Technik GmbH, Germany) were mixed in the desired molar ratios for 3 h with a Turbula mixer (Willy A. Bachofen AG Maschinenfabrik, Type T2C, Switzerland) using ZrO_2 balls with a diameter of 5 mm. Next, the powder mixtures were densified and sintered in a spark plasma sintering (SPS) furnace (FCT SPS system, type KCE-FCT HP D-25-SI, Germany) at 1500 °C with a heating rate of 20 °C·min⁻¹. A pressure of 50 MPa was applied till the temperature reached 600 °C. Then, the pressure was released to avoid leakage of melted Al. When the temperature reached to 1500 °C, the pressure of 50 MPa was applied again to promote alloying and densification. The sample was kept for 30 min. at the sintering temperature and thereafter naturally cooled to room temperature.

The sintered $\text{Mo}(\text{Al}_x\text{Si}_{1-x})_2$ alloys exhibit crystal lattice changes from hexagonal type C40 to orthorhombic type C54 with increasing Al content; see Section 2.1. The actual composition and the phase fractions of the alloy bulk samples analysed with electron probe X-ray microanalysis (EPMA) and X-ray diffractometry (XRD) are listed in Table 1.

2.2.2. Preparation of $\text{Mo}(\text{Al}_x\text{Si}_{1-x})_2$ particles

After sintering, the discs (20 mm diameter and 3 mm thickness) were crushed with a Fritsch Pulverisette (type P-0150, Germany). Two different size fractions of the particles were prepared by sieving (Analysensieb, DIN-ISO 3310-1, Retsch, Germany), namely fine particles of size $D < 20 \mu\text{m}$ and coarse particles of size $D > 20 \mu\text{m}$. The fine powder fraction was discarded due to the manufacturing constraints when using plasma spraying to fabricate the self-healing TBC [16]. Then, small particles will evaporate during plasma spraying and large particles will not be melted. Moreover, small particles do not contain sufficient amount of Al for encapsulation; see Section 3.1. To polish away the sharp edges of the crushed particles with a size of $D > 20 \mu\text{m}$, a planetary ball mill (PM100, Retsch GmbH, Germany) was used. To this end, a 50 ml zirconia jar with 200 and 90 balls with diameters of 3 and 5 mm zirconia balls were used. As polishing medium SiC (99.8%, 1 μm , Alfa Aesar, Germany) was used and mixed with about 25 ml isopropanol. Several batches of about 5.5 g of powder were milled with a rotation speed of 100 rpm for 100 minutes which was realized by cycles of milling and pause for 25 and 5 minutes, respectively. Next, the milled particles were washed with deionized water (Milli Q, 18.2 M Ω ·cm at 25 °C) and sieved with a 20 μm mesh sieve to remove the fine particles and the milling media. The remaining particles were dried in an oven at 80 °C overnight. Then, the particles were passed through a 50 μm sieve to eliminate the coarse fraction. Finally, the particles with a size of $20 < D < 50 \mu\text{m}$ were obtained. The morphology of the as prepared particles is shown in Fig. 3.

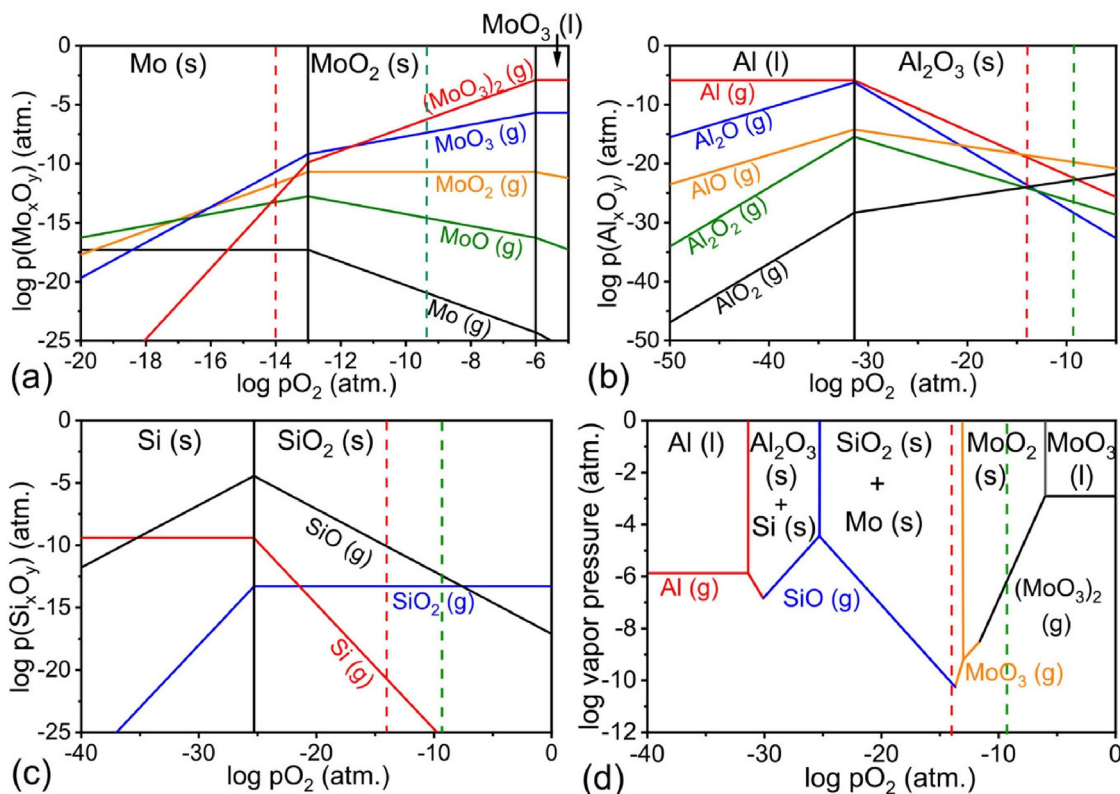


Fig. 2. Stability diagrams at 1100 °C for: (a) Mo–O; (b) Al–O; (c) Si–O; and (d) combined volatility diagram, illustrating the highest vapor pressure of the various gaseous species as a function of different p_{O_2} . The dashed red and green lines indicate an oxygen partial pressure of 10^{-14} atm. and 5×10^{-10} atm., respectively. (For interpretation of the references to colour in this figure legend, the reader is referred to the web version of this article.)

Table 1

Chemical composition and constituting phases of Mo(Al_xSi_{1-x})₂ materials prepared by SPS.

Actual x	Al fraction* (at.%)	Phase fraction (wt.%)	Crystal lattice (-)
0.35	23.5 ± 0.5	H: 100.0	C40
0.40	26.4 ± 0.4	H: 100.0	C40
0.48	31.9 ± 0.1	H: 92.8 O: 7.2	C40 C54
0.52	34.9 ± 3.5	H: 5.4 O: 14.6	C40 C54
0.58	38.9 ± 0.3	H: 5.7 O: 90.2 T: 4.1	C40 C54 D8M
0.65	43.1 ± 0.5	O: 92.7 T: 7.3	C54 D8M

H: hexagonal Mo(Al,Si)₂; O: orthorhombic Mo(Al,Si)₂; T: tetragonal Mo₅Si₃; analysed by Rietveld refinement with MAUD software.

* As determined with EPMA, cf. Section 2.2.

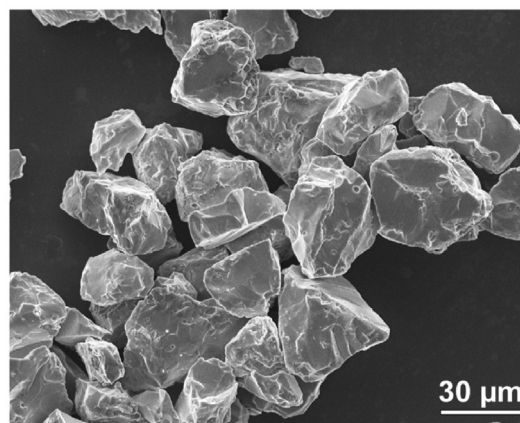


Fig. 3. SEM image showing morphology of the Mo(Al,Si)₂ particles after milling, sieving and polishing treatment.

2.2.3. Oxidation experiments

The Mo(Al_xSi_{1-x})₂ particles were oxidized in gas mixtures of Ar + 8 vol.% CO₂ + 50 vol.% CO and Ar + 95 vol.% CO₂ + 2.5 vol.% CO at 1100 °C, corresponding with oxygen partial pressures (p_{O_2}) of 10^{-14} and 5×10^{-10} atm., respectively. Also, oxidation of the as-prepared Mo(Al_xSi_{1-x})₂ particles was conducted in dry synthetic air. The kinetics of isothermal oxidation were monitored with thermogravimetric analysis (TGA) using a dual furnace balance (Seteram TAG 16/18, France), which allows automatic correction for buoyancy effects. The alumina furnace tubes have an inner diameter 15 mm. This analyser is equipped with Pt/Pt-10 %Rh (S-type) thermocouples. The gas mixture was admitted to the TGA analyser via mass flow controllers (Bronkhorst, the Netherlands)

operated with Labview (version 2020) such that the total gas flow matches 80 sccm¹ which was equally divided over both furnace tubes. The gases of Ar, CO and CO₂ were supplied by Linde Gas Benelux BV (purity better than 5N). Prior to admitting the gas mixture, Ar was filtered to remove any residual moisture and hydrocarbons, with an SGT click on oxygen trap (< 5 ppb O₂, SGT Middelburg, The Netherlands), Hydrosorb (< 20 ppb H₂O) and Accosorb (< 10 ppb hydrocarbons) filters (Messer Griesheim, Germany), respectively.

¹ standard cubic centimetres per minute.

The as-prepared alloy particles were mixed with yttria partially stabilized zirconia (YPSZ, Amprit 827, H.C. Starck, Germany) with a mass ratio of 1:3 to avoid bonding and sintering at high temperature ensuring uniform oxidation of all particles in a 100 μL alumina crucible. The alumina crucible was first filled with about 50 mg of the free alloy particles using a Mettler Toledo mechanical balance (AG-204, Switzerland, accuracy $\pm 1 \mu\text{g}$). Next, the YPSZ particles were added to the crucible until the total mass reached 200 mg. Then, this crucible with the powder mixture was placed onto a vibrator (Henry Schein, Vibrator L, Germany) to attain a homogeneous distribution of the particles. Finally, the crucible with the particles was mounted at one side of the TGA balance and an identical but empty crucible at the other side of the balance. To flush the gas lines, balance and furnaces, the TGA system was pumped to vacuum ($<50 \text{ Pa}$) and refilled with Ar, which was repeated three times. Thereafter, the dual furnaces were heated from room temperature to the target temperature with $10 \text{ }^\circ\text{C}\cdot\text{min}^{-1}$, while purging with 80 sccm Ar, i.e., 40 sccm gas through each furnace. When the target temperature for isothermal oxidation was reached, the gas composition was switched to the oxidation atmosphere (see above) while maintaining a total gas flow of 80 sccm for 16 h. After oxidation, the furnace was cooled to room temperature with $20 \text{ }^\circ\text{C}\cdot\text{min}^{-1}$ while flushing with pure Ar.

With the same procedure as described above, isothermal oxidation of the particles at different temperatures, i.e., 1050 and 1075 $^\circ\text{C}$, were performed in order to evaluate the activation energy of oxidation with p_{O_2} of 10^{-14} and $5 \times 10^{-10} \text{ atm.}$, respectively. The $\text{Mo}(\text{Al}_x\text{Si}_{1-x})_2$ particles were oxidized in gas mixtures of: Ar + 21 vol.% CO_2 + 50 vol.% CO at 1050 $^\circ\text{C}$ and Ar + 13 vol.% CO_2 + 50 vol.% CO at 1075 $^\circ\text{C}$ corresponding to a p_{O_2} of 10^{-14} , and Ar + 97.9 vol.% CO_2 + 1.06 vol.% CO at 1050 $^\circ\text{C}$ and Ar + 96.7 vol.% CO_2 + 1.7 vol.% CO at 1075 $^\circ\text{C}$ corresponding to a p_{O_2} of $5 \times 10^{-10} \text{ atm.}$

The high temperature stability of the encapsulated particles (with a low p_{O_2} oxidation) was investigated by exposure to a high p_{O_2} (Ar with 20 vol.% O_2) at 1100 $^\circ\text{C}$. For this purpose, TGA was employed as well. When the encapsulation in Ar/CO/ CO_2 atmosphere was completed, the gas was switched directly to Ar + 20 vol.% O_2 , for another 50 h. Finally, the furnace was cooled to room temperature in pure Ar.

2.2.4. Characterization

The phase composition of the materials was determined with X-ray diffractometry (XRD) using a D8 advance diffractometer (Bruker, Germany) operated with Cu $K\alpha$ radiation. Particles were deposited on a Si-(510) single crystal wafer (University Wafer, USA). Diffractograms were recorded in the 2θ range of 10 to 110 $^\circ$ with a 2θ step size of 0.030 $^\circ$ and a counting time per step of 2 s. These diffractograms were evaluated using the Bruker Diffrac EVA software (version 3.1).

The microstructure and the morphology of the particles was observed with scanning electron microscopy (SEM) using a JEOL JSM 6500F (JEOL, Japan). This instrument is equipped with an ultra-dry energy dispersive spectrometer (EDS) for X-ray micro analysis (XMA) using System 7, Thermo Fisher Noran, USA. In addition, SEM combined with a xenon plasma focused ion beam (Helios G4 PFIB UXe, Thermo Fisher Scientific, USA) was performed to create cross-sections of the oxidized particles. This instrument is equipped with an EDAX system for energy dispersive X-ray micro analysis (XMA) with an Octane Elite plus detector, using TEAM acquisition and analysis software (version 4.5). First, the particles to be investigated were placed on a single crystal silicon wafer (Si-(001) p-type, University Wafer, USA). Subsequently, one of the particles was covered with about 2 μm layer of Pt doped with C. Then, the particle was cut with the xenon plasma focused ion beam (PFIB) operated at 30 keV. Finally, the surface of the particle

cross-section was polished with a low current Xe ion beam. Transmission electron microscopy (TEM) lamella from selected area in the oxide scale prepared with the plasma focused ion beam were lifted. The grain morphology was observed with scanning transmission electron microscopy (STEM) within the dual beam microscope (Helios G4 PFIB UXe, Thermo Fisher Scientific, USA) operated with a 30 keV electron beam. Subsequently, the thin lamellas were analysed with TEM using a JEOL JEM-1400 plus (JEOL, Japan) operated with a 120 keV electron beam.

3. Results and discussion

3.1. Design of $\text{Mo}(\text{Al}_x\text{Si}_{1-x})_2$ as healing particles

It is conceived that by oxidation of $\text{Mo}(\text{Al}_x\text{Si}_{1-x})_2$ a closed shell of alumina ($\alpha\text{-Al}_2\text{O}_3$) with a core of Mo-Si will be formed. For the application on hand, design of these particles is prerequisite.

3.1.1. Shell thickness

Assuming that the $\text{Mo}(\text{Al}_x\text{Si}_{1-x})_2$ particle has a spherical shape with a diameter d , the Al_2O_3 shell has a uniform thickness δ and considering that all Al is consumed by selective oxidation, then the thickness of the alumina shell can be calculated according to [7]:

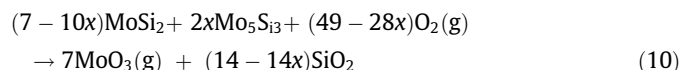
$$\delta = \frac{d}{2} \left[\left(1 + \frac{xM_s\rho_p}{M_p\rho_s} \right)^{\frac{1}{3}} - 1 \right] \quad (9)$$

where M_p and M_s denote the molecular weights, ρ_p and ρ_s the densities of the particle and the shell, respectively.

The explicit relation between the alumina shell thickness δ and the diameter d of the healing particle is displayed in Fig. 4a for different fractions x of Al. When applying a TBC with plasma spraying, the diameter of the healing particle should be about 20 to 50 μm due to manufacturing constraints [16,32–34]. For example, when targeting for a minimum alumina shell thickness of 1 μm by full Al depletion of the particles with a diameter of 30 μm , then the minimum Al fraction x according to Eq. (9) should be 0.2; see Fig. 4a.

3.1.2. Volume expansion

After alloying MoSi_2 with Al by replacing Si, part of the volume expansion associated with the healing reaction is sacrificed. The relative volume expansion (RVE) of the healing particle, after all the Al is consumed by selective oxidation of $\text{Mo}(\text{Al}_x\text{Si}_{1-x})_2$, cf. Section 2.1, can be estimated by considering the oxidation induced healing reaction:



Then, for associated relative volume expansion can be written:

$$\text{RVE} = \left[\frac{(14 - 14x)V_{\text{SiO}_2}}{(7 - 10x)V_{\text{MoSi}_2} + 2xV_{\text{Mo}_5\text{Si}_3}} - 1 \right] \times 100\% \quad (11)$$

where V_{SiO_2} is the molar volume of 28.9 cm^3 for amorphous SiO_2 , $V_{\text{Mo}(\text{Al},\text{Si})_2}$ of 24.3 cm^3 for $\text{Mo}(\text{Al},\text{Si})_2$ and $V_{\text{Mo}_5\text{Si}_3}$ of 68.8 cm^3 for Mo_5Si_3 . Although the RVE decreases with increasing Al content, the oxidation reaction still exhibits a large positive volume expansion, i.e., $\text{RVE} \geq 40 \%$ for $x \leq 0.65$, which indicates a strong healing ability; see Fig. 4b.

3.2. Direct exposure of $\text{Mo}(\text{Al},\text{Si})_2$ particles to dry air at 1100 $^\circ\text{C}$

When particles with the composition of $\text{Mo}(\text{Al}_{0.40}\text{Si}_{0.60})_2$ are exposed to dry synthetic air at 1100 $^\circ\text{C}$ for 16 h, the oxidation

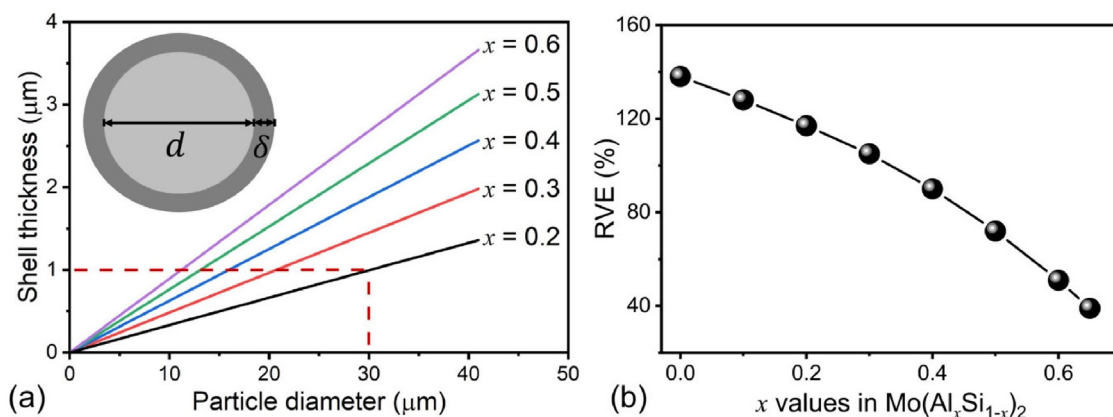


Fig. 4. (a) Relationship between the alumina shell thickness and the size of Mo(Al_xSi_{1-x})₂ spherical healing particle for different compositions; (b) relationship between the Al content in Mo(Al_xSi)₂ and the relative volume expansion in the healing reaction.

results in a rather porous oxide scale; see Fig. 5a. Besides Al₂O₃ also SiO₂ is formed according to XMA. Initially, a rapid mass gain was recorded, which is associated with the formation of both Al₂O₃ and SiO₂; see Fig. 5b. However, the predicted mass gain for full oxidation of Al according to Eq. (1) is much larger than recorded as indicated in Fig. 5b, which suggests that the mass change is accompanied by the formation of volatile MoO₃ [35]; cf. Fig. 2. Subsequently, the mass loss due to the formation of volatile MoO₃ was recorded. Thus, the porous oxide shell structure does not protect the core of the particle from oxidation. Hence, oxidation in a low pO₂ ambient as a precursor for the formation of an exclusive Al₂O₃ scale was performed. In the sequel, the results of this work are reported.

It is noted that the oxidation behaviour of the particle is completely different compared with oxidation of bulk Mo(Al_{0.40}Si_{0.60})₂ under the same conditions [36]. Then, a closed and protective scale of α-Al₂O₃ is formed under these conditions. In that case the 'reservoir' of Al is virtually infinite and the diffusion of Al in the alloy is sufficiently fast.

3.3. Encapsulation of Mo(Al_xSi_{1-x})₂ particles by oxidation with low pO₂

The X-ray diffraction patterns of the Mo(Al_xSi_{1-x})₂ particles mixed with YPSZ granules after oxidation at 1100 °C with a pO₂ of 10⁻¹⁴ atm. for 16 h are shown in Fig. 6. Although peaks from YPSZ are dominant in the patterns, lines pertaining to α-Al₂O₃

and Mo₅Si₃ were identified. These two phases are the result of thermal oxidation of the Mo(Al_xSi_{1-x})₂ particles. Also remanent Mo(Al_xSi_{1-x})₂ was recognized in the XRD patterns. However, this phase exhibits a hexagonal crystal lattice. Thus, the initially present orthorhombic Mo(Al_xSi_{1-x})₂ phase in the high Al containing particles (cf. Table 1) is transformed into hexagonal Mo(Al_xSi_{1-x})₂ due to Al depletion upon high temperature oxidation.

All Mo(Al_xSi_{1-x})₂ particles with different Al content features the same surface morphology after oxidation at 1100 °C with a pO₂ of 10⁻¹⁴ atm. for 16 h. As an example, the surface morphology of a free particle covered with thermally grown oxide is shown in Fig. 7a–c. The oxide scale is exclusively composed of α-Al₂O₃ according to XMA and XRD. Two different oxide morphologies can be observed (see Fig. 7a): flaky oxides forming network shaped ridges (see Fig. 7b), and in between compact oxides (see Fig. 7c). The particles are fully covered with an alumina shell with a thickness of about 0.8 ± 0.3 μm after oxidation at 1100 °C with a pO₂ of 10⁻¹⁴ atm. for 16 h, as can be seen in a cross section of a free particle; see Fig. 8a. The Al depletion layer composed of Mo₅(Al₃Si)₃ adjacent to the alumina layer can also be observed; see Fig. 8b. A composition depth profile confirms the presence of the different layers from the surface to the core of the particles after oxidation in the low pO₂ ambient at 1100 °C for 16 h; see Fig. 8c. The atomic ratio in the oxide scale represents the exclusive formation of Al₂O₃. The Mo₅(Al₃Si)₃ depletion layer contains about 3.6 at.% Al, while the core contains still high Al fraction; cf. Fig. 8c. The formation of

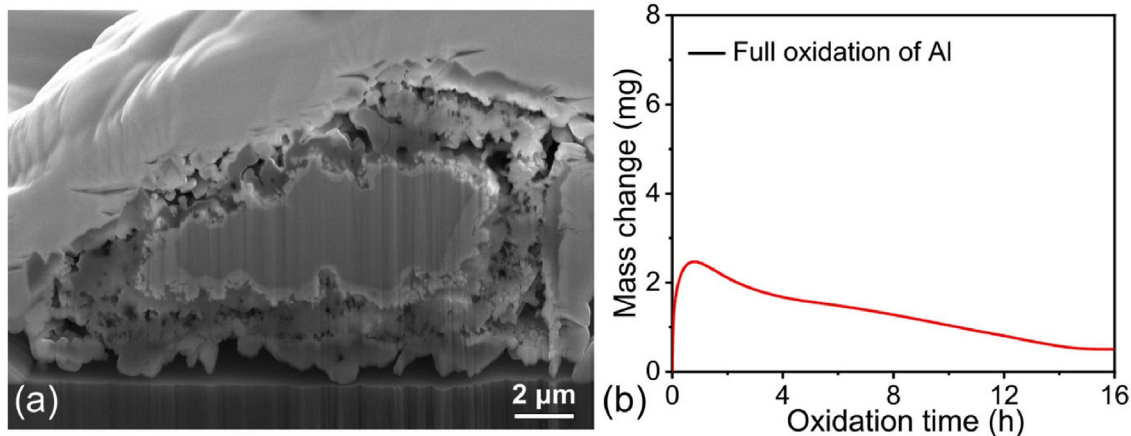


Fig. 5. Mo(Al_{0.40}Si_{0.60})₂ particle after oxidation in Ar with 20 vol.% O₂ at 1100 °C for 16 h: (a) SEM image of a cross-section; (b) mass change. The mass gain corresponding with full oxidation of Al only is indicated.

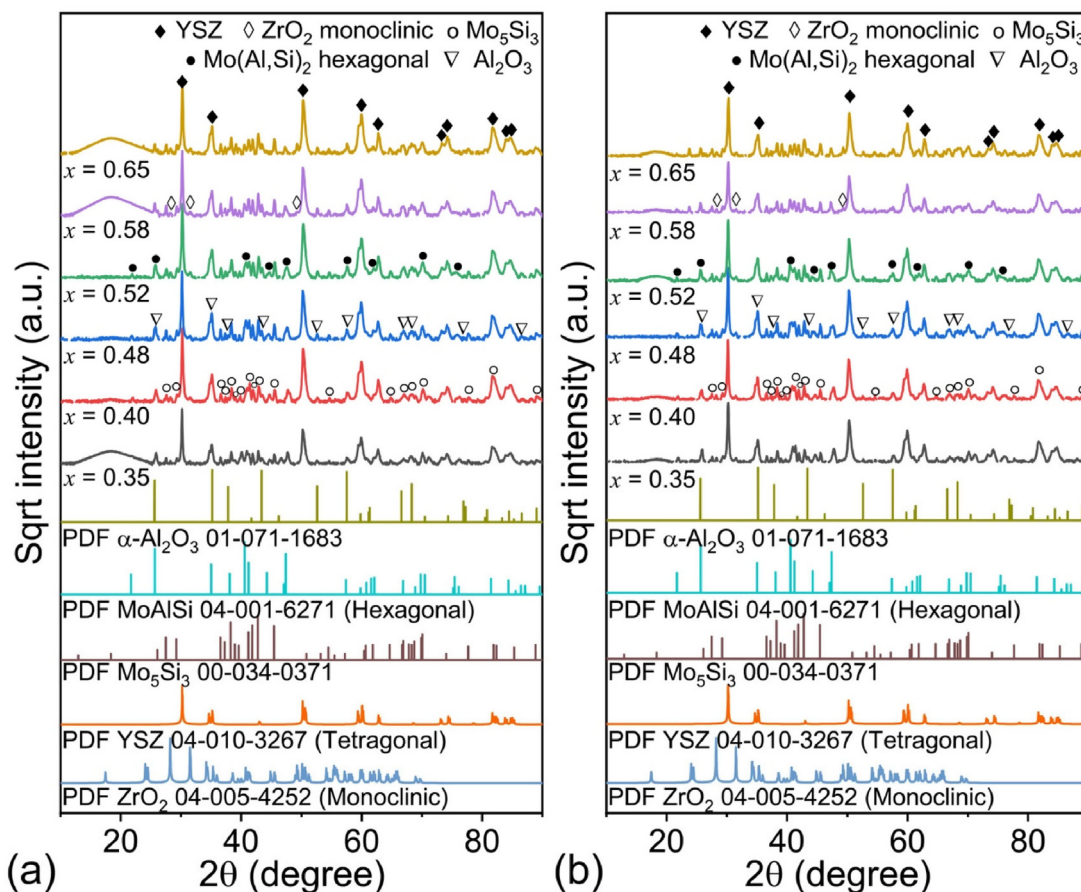


Fig. 6. XRD patterns of the $\text{Mo}(\text{Al}_x\text{Si}_{1-x})_2$ free particles mixed with YPSZ after oxidation with an oxygen partial pressure of (a) 10^{-14} atm. and (b) 5×10^{-10} atm. at 1100°C for 16 h.

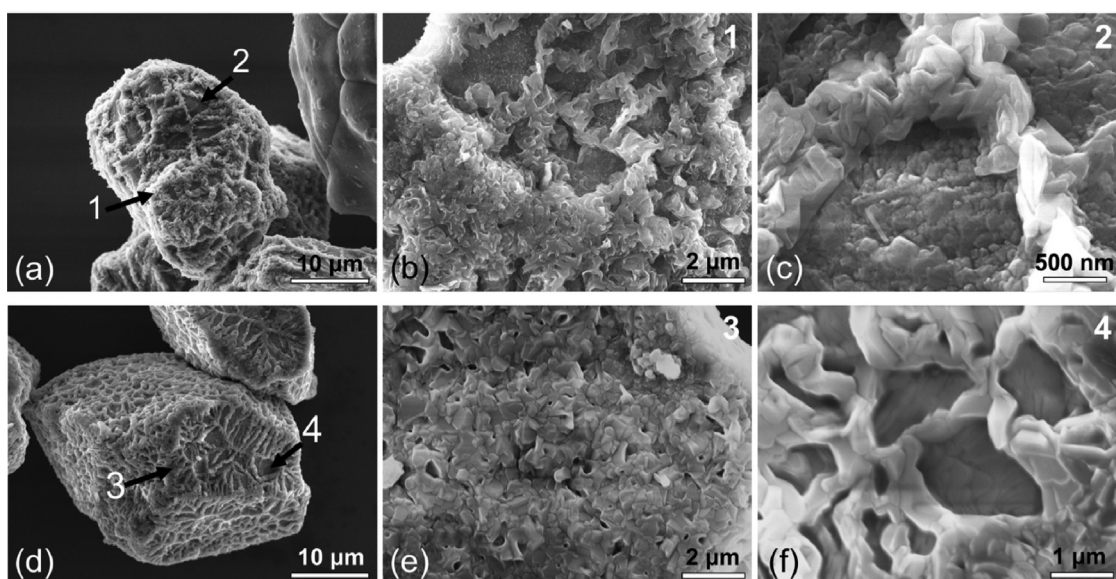


Fig. 7. SEM images showing morphology of a $\text{Mo}(\text{Al}_{0.40}\text{Si}_{0.60})_2$ particle after oxidation with an oxygen partial pressure of (a)–(c) 10^{-14} atm. and (d)–(f) 5×10^{-10} atm., both at 1100°C for 16 h: (a) a whole particle; (b) flaky oxide location indicated with arrow 1 in (a); (c) compact oxide location indicated with arrow 2 in (a); (d) a whole particle; (e) flaky oxide location indicated with arrow 3 in (c); (f) compact oxide location indicated with arrow 4 in (c).

$\text{Mo}_5(\text{Al,Si})_3$ phase is due to the oxidation reaction of Al at the alloy/gas interface, viz. Eq. (1), which is consistent with the depletion path indicated in Fig. 1b, and the content of Al in the $\text{Mo}_5(\text{Al,Si})_3$

Si_3 depletion layer is in agreement with the Mo–Al–Si phase diagram at 1100°C ; see Fig. 1b. The microstructure of the alumina scale formed exhibits a two-layer microstructure; see Fig. 8d. A

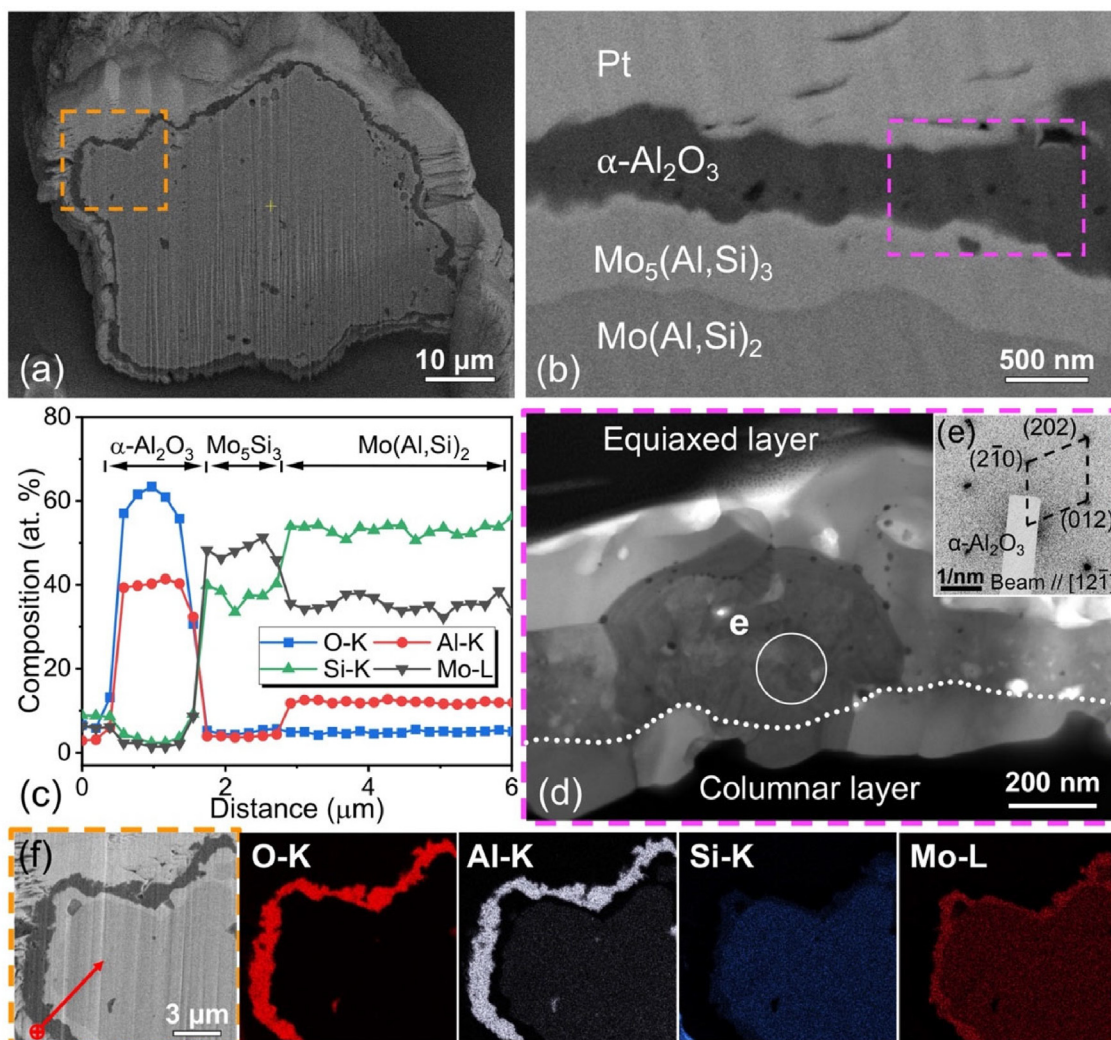


Fig. 8. Cross-section of $\text{Mo}(\text{Al}_{0.40}\text{Si}_{0.60})_2$ particle after oxidation with an oxygen partial pressure of 10^{-14} atm. at 1100°C for 16 h: (a) SEM image; (b) detail BSE image of the shell and adjacent matrix of the particle with $\alpha\text{-Al}_2\text{O}_3$ being the oxide shell, $\text{Mo}_5(\text{Al,Si})_3$ being the depleted layer and $\text{Mo}(\text{Al,Si})_2$ being the core; (c) composition profile along the path indicated by the red arrow in (f); (d) STEM image of the oxide shell of $\alpha\text{-Al}_2\text{O}_3$ (the dotted curve is to distinguish the grain morphologies in the upper and lower part of the oxide shell). The lower part of the oxide shell exhibits an equiaxed grain morphology and the upper part has columnar grains, which correspond to Al outward-diffusion dominant and O inward-diffusion dominant growth, respectively; (e) selected-area electron diffraction pattern (SAEDP) of corresponding area indicated in (d); (f) X-ray emission maps of O, Al, Si and Mo, respectively; location indicated with the frame box in (a). (For interpretation of the references to colour in this figure legend, the reader is referred to the web version of this article.)

thin layer of columnar grains is grown adjacent to the core of the particle, while a layer of equiaxed grains is formed at the surface in contact with the gaseous ambient. A combination of selected-area electron diffraction patterns (SAEDPs, Fig. 8e) and X-ray elemental mapping (Fig. 8f) confirms the exclusive formation of a continuous $\alpha\text{-Al}_2\text{O}_3$ layer encapsulating the $\text{Mo}(\text{Al}_x\text{Si}_{1-x})_2$ particles.

A similar surface morphology was observed when the $\text{Mo}(\text{Al}_x\text{Si}_{1-x})_2$ particles were oxidized at 1100°C with a $p\text{O}_2$ of 5×10^{-10} atm. for 16 h; see Fig. 7d–f. As compared to oxidation with a $p\text{O}_2$ of 1×10^{-14} atm., the ridges on top of the compact oxides can still be observed (see Fig. 7d) and the flaky oxides appear denser (see Fig. 7e and 7f). The oxidation of the $\text{Mo}(\text{Al}_x\text{Si}_{1-x})_2$ particles with a $p\text{O}_2$ of 5×10^{-10} atm. at 1100°C , which is beyond the dissociation oxygen partial pressure of solid MoO_2 (see Fig. 2a), results also in exclusive formation of a continuous $\alpha\text{-Al}_2\text{O}_3$ shell; see Fig. 9a–d. Apparently, under these oxidation condition the formation of the volatile species MoO_3 or $(\text{MoO}_3)_2$ are mitigated once the surface of the $\text{Mo}(\text{Al}_x\text{Si}_{1-x})_2$ particles is completely covered with $\alpha\text{-Al}_2\text{O}_3$. The alumina layer of $\text{Mo}(\text{Al}_{0.40}\text{Si}_{0.60})_2$ particle is thicker when oxi-

dized in an ambient with $p\text{O}_2$ of 5×10^{-10} atm. as compared with oxidation with $p\text{O}_2$ of 10^{-14} atm. at 1100°C for 16 h, i.e., about 1.3 ± 0.2 versus 0.8 ± 0.3 μm . The Al depletion layer composed of $\text{Mo}_5(\text{Al,Si})_3$ can be observed clearly; see Fig. 9. The exclusive formation of continuous $\alpha\text{-Al}_2\text{O}_3$ layer encapsulating the $\text{Mo}(\text{Al}_{0.40}\text{Si}_{0.60})_2$ particles is confirmed by X-ray elemental mapping; see Fig. 9c. This oxide layer features a distinct two-layered structure, viz. a dense equiaxed layer on top of a dense columnar layer; see Fig. 9b. Composition analysis with XMA shows that still a high amount of Al is present in the centre of the particle (Fig. 9d), namely 22.3 at.% compared with 26.4 at.% initially.

3.4. The growth kinetics of alumina scale

The converted fraction of $\text{Mo}(\text{Al}_x\text{Si}_{1-x})_2$ particles into Al_2O_3 due to oxidation at 1100°C with a $p\text{O}_2$ of 10^{-14} atm. as a function of time is displayed in Fig. 10a. Fast oxidation during the initial stage of oxidation can be observed for all the $\text{Mo}(\text{Al}_x\text{Si}_{1-x})_2$ particle compositions and then followed by a slow steady conversion. The fast

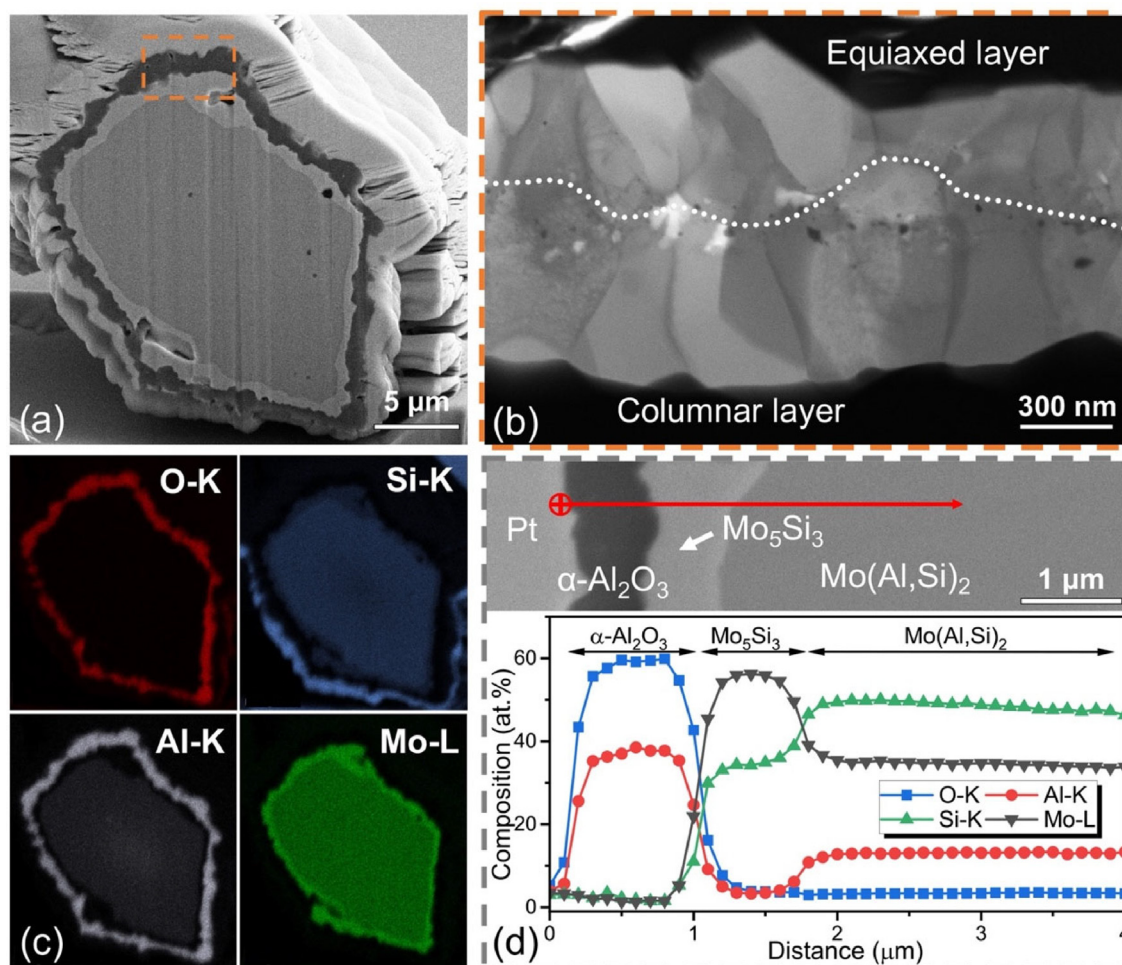


Fig. 9. Cross-section of $\text{Mo}(\text{Al}_{0.40}\text{Si}_{0.60})_2$ particle after oxidation with an oxygen partial pressure of 5×10^{-10} atm. at 1100°C for 16 h: (a) SEM image; (b) STEM image of the oxide shell of $\alpha\text{-Al}_2\text{O}_3$ (the dotted curve is to distinguish the grain morphologies in the upper and lower part of the oxide shell). The lower part of the oxide shell exhibits an equiaxed grain morphology and the upper part has columnar grains, which correspond to Al outward-diffusion dominant and O inward-diffusion dominant growth, respectively; (c) X-ray emission maps of O, Al, Si and Mo, respectively; (d) composition profile along the path indicated by the red arrow. (For interpretation of the references to colour in this figure legend, the reader is referred to the web version of this article.)

initial oxidation is likely associated with a not yet continuous oxide shell around the particle.

A higher conversion rate was observed during the steady oxidation stage when oxidized with a $p\text{O}_2$ of 5×10^{-10} atm., as compared with oxidation with a $p\text{O}_2$ of 1×10^{-14} atm.; see Fig. 10a and 10b. For both cases it holds that the converted fraction is practically independent of the aluminium content (x) of the original particles. This is somewhat different from the oxidation of bulk $\text{Mo}(\text{Al,Si})_2$ under the same conditions [36]. Then, the oxidation was slightly accelerated with increasing Al content in the original material. This difference may be attributed to the infinite supply of Al to the surface of the bulk alloys maintain a high Al interface concentration depending on the alloy's Al content, while the particles become depleted of Al resulting in a relatively low Al interface concentration virtually independent of the original Al content.

The prevailing reaction model was determined from the reduced-time plot (cf. Section 2.3) made for the converted fraction of $\text{Mo}(\text{Al}_{0.48}\text{Si}_{0.52})_2$ particles oxidized with $p\text{O}_2$ of 10^{-14} atm. and 5×10^{-10} atm. at 1100°C ; see Fig. 10c and 10d. Out of the various reaction models, the 3-D diffusion-Jander (D3) model closely resembles the experimental data (R^2 equals to 0.9933 and 0.9827 for $p\text{O}_2$ of 10^{-14} atm. and 5×10^{-10} atm., respectively), demonstrating a diffusion-controlled oxidation process. The integral form of this model is defined as:

$$g(\alpha) = (1 - (1 - \alpha)^{1/3})^2 \quad (12)$$

When combining Eq. (5)–(8) and (12), an expression representing the conversion α can be formulated as:

$$\alpha = 1 - (1 - \sqrt[3]{kt})^3 \quad (13)$$

The rate constant k has been determined from a linear least-square fitting of Eq. (6) to the isothermal oxidation kinetic data for each $\text{Mo}(\text{Al}_x\text{Si}_{1-x})_2$ particle composition with x from 0.35 to 0.65; see Supplementary Material 1.2. The oxidation rate constant as a function of the Al content of the original particles (cf. Fig. 10e) confirms the faster oxidation kinetics with a $p\text{O}_2$ of 5×10^{-10} atm. as compared to that with a $p\text{O}_2$ of 10^{-14} atm. The oxidation rate constant k is practically independent of the Al content of the original particles regardless the $p\text{O}_2$ of the gas ambient (see above).

Activation energy of the oxidation in the $p\text{O}_2$ of 10^{-14} atm. and 5×10^{-10} atm. were evaluated according to Eq. (8); see Fig. 10f. The activation energy equals to 184 ± 22 kJ/mol and 83 ± 11 kJ/mol for the oxidation in the $p\text{O}_2$ of 5×10^{-10} atm. and 10^{-14} atm., respectively. These activation energies for the thermal oxidation of the $\text{Mo}(\text{Al,Si})_2$ particles are lower than that for the thermal oxidation of the bulk $\text{Mo}(\text{Al,Si})_2$ alloys (310 kJ/mol [29,37]) and other high temperature alumina forming alloys, e.g., Ti_2AlC (250 kJ/mol

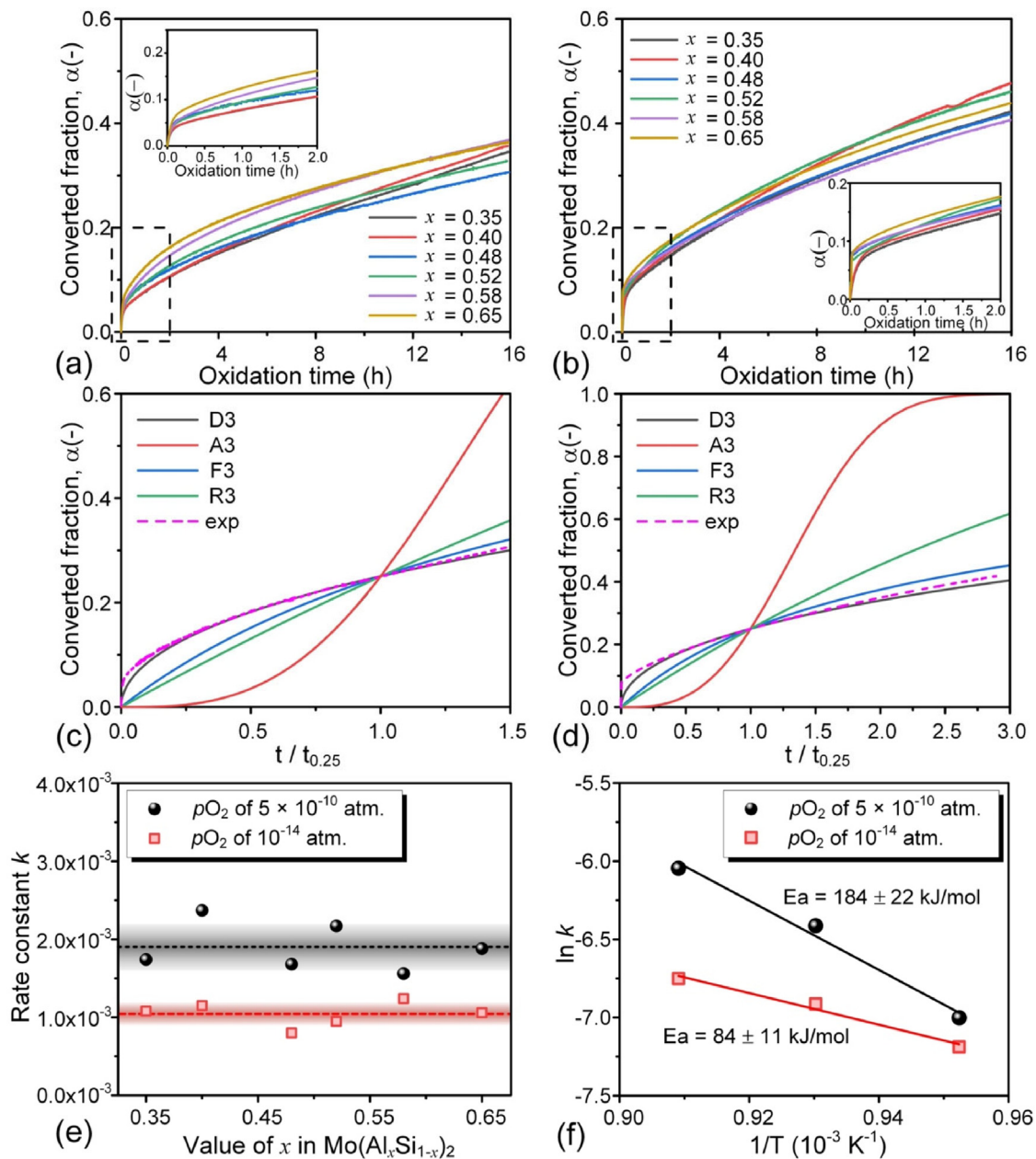


Fig. 10. Oxidation kinetics in terms of converted fraction versus oxidation time of (a) $\text{Mo}(\text{Al}_x\text{Si}_{1-x})_2$ particles with an oxygen partial pressure of 10^{-14} atm. at 1100 °C for 16 h, and (b) $\text{Mo}(\text{Al}_x\text{Si}_{1-x})_2$ particles with an oxygen partial pressure of 5×10^{-10} atm. at 1100 °C for 16 h. Reduced time plots of the converted fraction α for various reaction models (cf. Supplementary Material 1.1) and experimental data of $\text{Mo}(\text{Al}_{0.48}\text{Si}_{0.52})_2$ particles oxidized with an oxygen partial pressure of (c) 10^{-14} atm. and (d) 5×10^{-10} atm., respectively. (e) Rate constant of $\text{Mo}(\text{Al}_x\text{Si}_{1-x})_2$ particles oxidized with an oxygen partial pressure of 10^{-14} atm. and 5×10^{-10} atm. at 1100 °C. (f) Rate constant of $\text{Mo}(\text{Al}_{0.4}\text{Si}_{0.6})_2$ particles oxidized with an oxygen partial pressure of 10^{-14} atm. and 5×10^{-10} atm. at temperature of 1050 °C, 1075 °C and 1100 °C for 16 h with the activation energies indicated.

[38]), FeCrAl and Ni_3Al alloys (240 kJ/mol [39]). The lower activation energy for the thermal oxidation of the $\text{Mo}(\text{Al},\text{Si})_2$ particles is likely due to the large number of surface defects (such as: dislocations, grain boundaries, steps and kinks, roughness, etc.), of which their number increases with surface area [40,41]. These surface defects promote the nucleation and growth of the oxide [40].

3.5. Growth mechanism of the alumina shell

The selective oxidation of Al in $\text{Mo}(\text{Al}_x\text{Si}_{1-x})_2$ created an $\alpha\text{-Al}_2\text{O}_3$ shell for the inner core material. The exclusive Al_2O_3 scale formed on $\text{Mo}(\text{Al}_x\text{Si}_{1-x})_2$ via selective oxidation process exhibits a distinct two-layered microstructure, which features a similar microstruc-

ture as observed in scales developed during oxidation of alumina forming alloys [20,42–44]. On the surface of the alloy, an oxide layer with columnar grains and equiaxed grains on top in contact with the gas ambient forms by selective oxidation of aluminium. A wedge-section technique was used first to illustrate the microstructure of Al_2O_3 scale formed on Fe-Cr-Al alloys [43]. In this oxide scale, the two-layered microstructure is due to a so-called “counter-diffusion process” along the grain boundaries [43,45]. The outward diffusion of aluminium governs the growth of the outer equiaxed layer, while the inward diffusion of oxygen determines the growth of the inner columnar layer interface [20,42–45].

In the present work, the same counter-diffusion mechanism is considered to be responsible for the growth of the alumina scale.

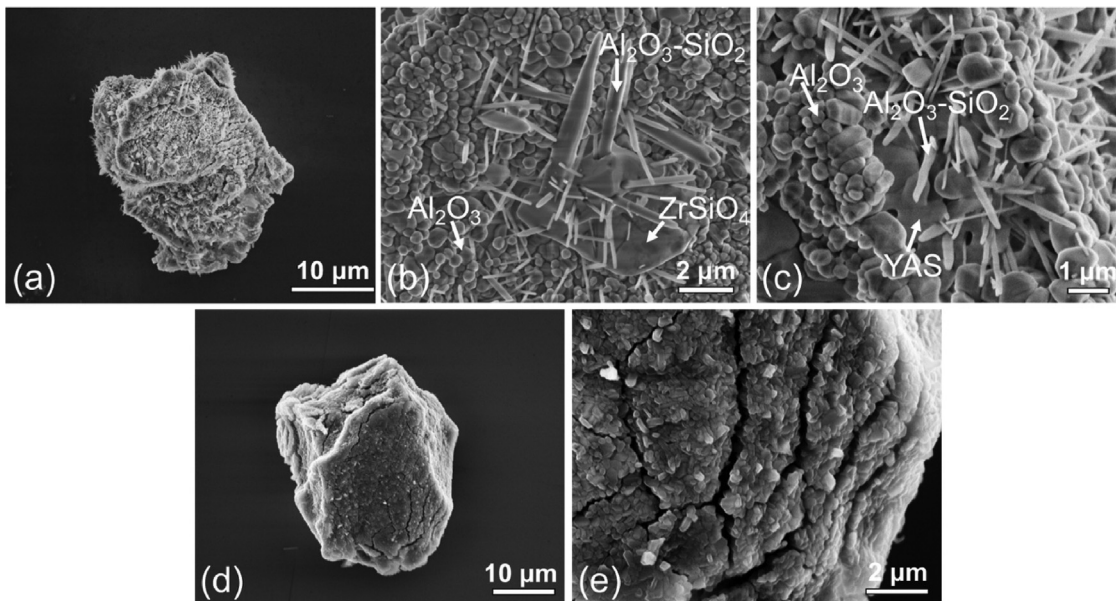


Fig. 11. SEM images of $\text{Mo}(\text{Al}_{0.40}\text{Si}_{0.60})_2$ particle after isothermal exposure at 1100 °C of $\text{Mo}(\text{Al}_{0.40}\text{Si}_{0.60})_2$ first with an oxygen partial pressure of (a)–(c) 10^{-14} atm. and (d)–(e) 5×10^{-10} atm. for 16 h followed with a high oxygen partial pressure (i.e., Ar with 20 vol.% O_2) for 50 h: (a) and (d) particle morphology; (b), (c) and (e) detail observation of surface oxides.

The observed flaky oxide at the surface creating network shaped bridges (cf. Fig. 7b and 7e), resembles to the equiaxed layer. This oxide is formed due to outward diffusion of Al along the grain

boundaries. The inner oxide layer, adjacent to the particle core, has a columnar grain structure and is formed by inward diffusion of oxygen. Comparing the oxide scale formed in the $p\text{O}_2$ of 10^{-14}

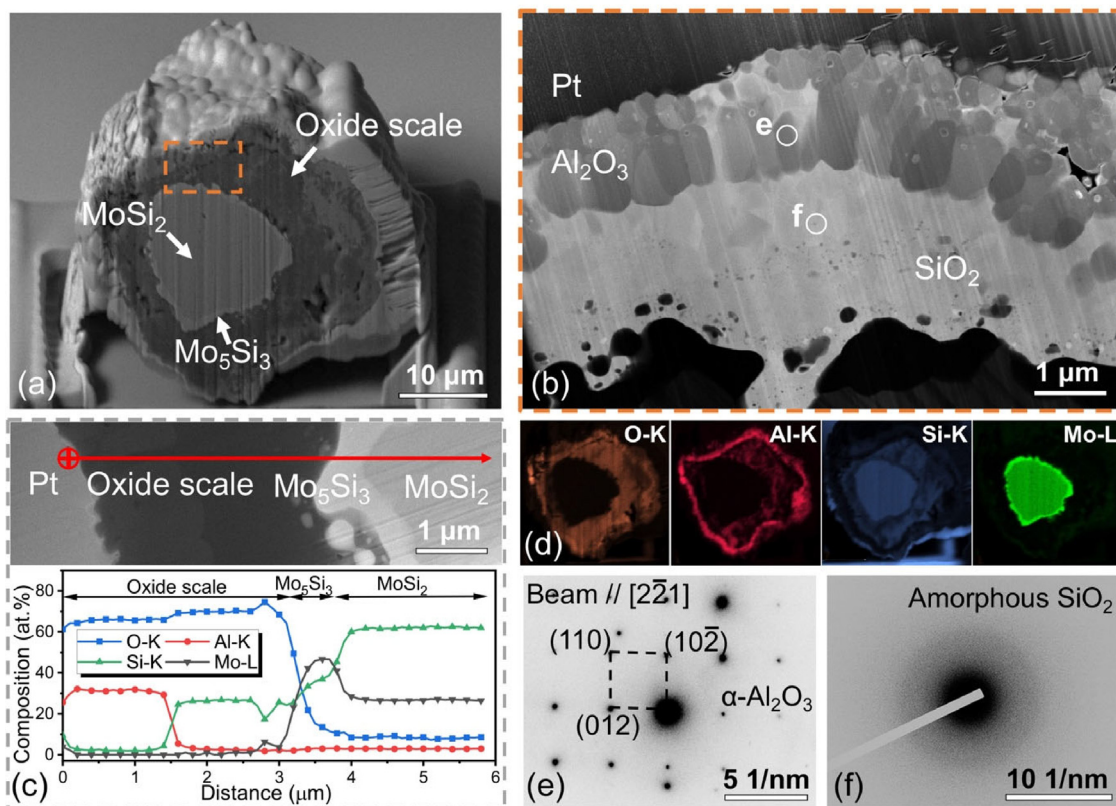


Fig. 12. Cross section of $\text{Mo}(\text{Al}_{0.40}\text{Si}_{0.60})_2$ particle after isothermal exposure at 1100 °C first with an oxygen partial pressure of 10^{-14} atm. for 16 h followed with a high oxygen partial pressure (i.e., Ar with 20 vol.% O_2) for 50 h. (a) SEM image; (b) STEM image on oxide scale; (c) composition profile along the path across the oxide scale, Mo_5Si_3 and MoSi_2 substrate indicated by the red arrow; (d) X-ray emission maps of O, Al, Si and Mo, respectively; (e) $\alpha\text{-Al}_2\text{O}_3$ and (f) amorphous SiO_2 . (For interpretation of the references to colour in this figure legend, the reader is referred to the web version of this article.)

atm. and 5×10^{-10} atm., it can be observed that the increase of oxygen partial pressure promotes the growth of both equiaxed and columnar grains; see Fig. 8d versus Fig. 9b. As a result, a denser oxide scale is formed in the pO_2 of 5×10^{-10} atm. compared to that formed in the pO_2 of 10^{-14} atm., which is the key for acting as a protective shell for the core of the particles.

3.6. Oxide shell stability

In typical applications, the oxygen partial pressure is high comparable to the air at atmospheric pressure (0.2 atm.) and can reach the embedded particles because the TBC exhibits an interconnected network of pores (about 20 vol.%) [1]. Therefore, particles were exposed at 1100 °C to Ar with 20 vol.% O_2 for 50 h to assess their long-term stability after pre-oxidation in a gas ambient with a pO_2 of 10^{-14} and 5×10^{-10} atm., respectively, for 16 h to form an exclusive alumina shell (cf. Section 4.3). For studying the oxide shell stability, particles of $Mo(Al_{0.40}Si_{0.60})_2$ were selected. The $Mo(Al_{0.40}Si_{0.60})_2$ has a single hexagonal crystal lattice structure; see Table 1.

3.6.1. Encapsulation with pO_2 of 10^{-14} atm.

The surface morphology shown in Fig. 11a confirms that the particles encapsulated with pO_2 of 10^{-14} atm. preserved their integ-

riety after exposure in Ar plus 20 vol.% O_2 at 1100 °C for 50 h. At the surface a granular oxide with needles and some cracks is observed; see Fig. 11a–c. The needle oxide is composed of $Al_2O_3-SiO_2$ according to XMA and corresponds with $3Al_2O_3 \cdot 2SiO_2$ according to the atomic ratio of the elements. This is confirmed by the XRD analysis, showing diffraction lines pertaining to mullite ($3Al_2O_3 \cdot 2SiO_2$) with an orthorhombic crystal lattice; see Supplementary Material 1.3. XRD analysis also showed diffraction lines corresponding with tetragonal $MoSi_2$, Mo_5Si_3 and $\alpha-Al_2O_3$; but no lines corresponding with crystalline SiO_2 . The tetragonal crystal lattice of $MoSi_2$ indicates that practically all Al in $Mo(Al_xSi_{1-x})_2$ has been consumed during oxidation, since Al can hardly be dissolved in the tetragonal $MoSi_2$; cf. Fig. 1. Further, due to the mixing of the $Mo(Al_xSi_{1-x})_2$ with yttria partially stabilized zirconia (cf. Section 2.2), small amounts of zircon ($ZrSiO_4$) [13] and yttrium aluminosilicate (YAS) [46,47] were formed on the surface of the particles during oxidation. These oxide phases can be recognized as island shaped species; see Fig. 11b and 11c.

After exposure in Ar plus 20 vol.% O_2 at 1100 °C for 50 h, a thick thermally grown oxide shell (about 7 μm) envelops the free particles encapsulated with a pO_2 of 10^{-14} atm. at 1100 °C for 16 h; see Fig. 12a. Composition analysis, elemental mapping and selected-area diffraction patterns confirm that oxide scale consists of an outer rim of $\alpha-Al_2O_3$ and an inner rim of amorphous SiO_2 ; see

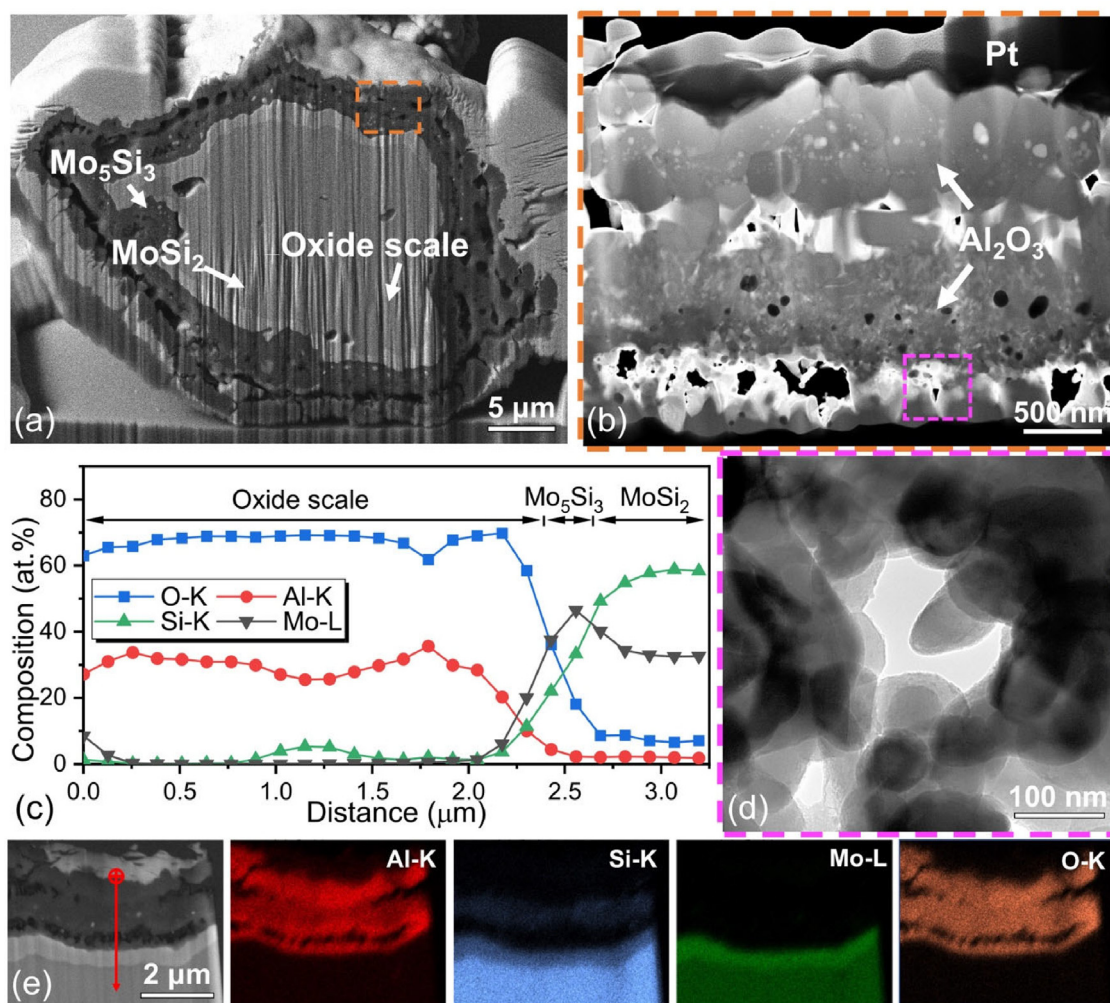


Fig. 13. Cross section of $Mo(Al_{0.40}Si_{0.60})_2$ particle after isothermal exposure at 1100 °C first with an oxygen partial pressure of 5×10^{-10} atm. for 16 h followed with an high oxygen partial pressure in dry synthetic air (i.e., Ar with 20 vol.% O_2) for 50 h. (a) SEM image; (b) STEM image of the oxide scale; (c) composition profile along the path indicated by the red arrow in (e); (d) bright-field TEM image of the oxide scale composed of fine grains; (e) X-ray emission maps of O, Al, Si and Mo, respectively. (For interpretation of the references to colour in this figure legend, the reader is referred to the web version of this article.)

Fig. 12b–f. The α - Al_2O_3 outer rim still exhibits a two-layered structure, but with significantly thickened columnar and equiaxed layer compared to the oxide shell formed after encapsulation in the $p\text{O}_2$ of 10^{-14} atm. for 16 h; see Fig. 8d and 12b. The SiO_2 underneath fills the gaps in the α - Al_2O_3 layer (Fig. 12b) and reacts with Al_2O_3 resulting into mullite ($3\text{Al}_2\text{O}_3 \cdot 2\text{SiO}_2$) as mentioned above. The core of the remnant particle is fully depleted of Al and is composed of pure MoSi_2 with a rim of Mo_5Si_3 ; see Fig. 12c and 12d. The two-layered structure of the α - Al_2O_3 in the outer rim indicates that the growth of Al_2O_3 still follows the counter diffusion mechanism when oxidizing in Ar with 20 vol.% O_2 after encapsulation. However, the SiO_2 formed by oxidation of the MoSi_2 core due to oxygen penetrating through the Al_2O_3 outer rim, indicates a limited protection provided by the Al_2O_3 shell formed by oxidation with a $p\text{O}_2$ of 10^{-14} atm. The Pilling-Bedworth ratio (PBR) of SiO_2/Si (2.26) is much larger than that of $\text{Al}_2\text{O}_3/\text{Al}$ (1.28) [48]. Therefore, the formation of silica is associated with a large volume expansion, which may have caused cracking of the Al_2O_3 shell [7]; see Fig. 11.

3.6.2. Encapsulation with $p\text{O}_2$ of 5×10^{-10} atm.

The integrity of the particles encapsulated with a $p\text{O}_2$ of 5×10^{-10} atm. and exposed to Ar plus 20 vol.% O_2 at 1100°C for 50 h is preserved; see Fig. 11d. As compared with the particles encapsulated with a $p\text{O}_2$ of 10^{-14} atm., no needle shaped oxide was observed at the surface (Fig. 11e) and the diffraction lines pertaining to mullite are very weak; see Supplementary Material 1.3.

An about $4 \mu\text{m}$ thick thermally grown oxide scale envelops the free particles encapsulated with $p\text{O}_2$ of 5×10^{-10} atm. after exposure in Ar plus 20 vol.% O_2 at 1100°C for 50 h; see Fig. 13a. This shell is significantly thinner (4 versus $7 \mu\text{m}$) than the shell formed on the particles pre-oxidized with a $p\text{O}_2$ of 10^{-14} atm. Composition analysis and elemental mapping confirm that the oxide scale consists almost exclusively of Al_2O_3 , and that the core of the remnant particle is fully depleted of Al and is composed of pure MoSi_2 with a rim of Mo_5Si_3 ; see Fig. 13c and 13e. The formation of an exclusive Al_2O_3 scale suggests that the encapsulation with $p\text{O}_2$ of 5×10^{-10} atm. at 1100°C for 16 h (cf. Section 3.3) acts as a strong barrier between the particle core material and the gaseous ambient at high temperatures. Two layers of Al_2O_3 are observed in the oxide scale formed after exposure in Ar with 20 vol.% O_2 at 1100°C for 50 h; see Fig. 13b. The Al_2O_3 outer layer still exhibits the two-layered structure formed by encapsulation with $p\text{O}_2$ of 5×10^{-10} atm. at 1100°C for 16 h (cf. Section 3.3) and the thickness of this layer remained the same after exposure to Ar with 20 vol.% O_2 at 1100°C for 50 h; see Fig. 13b and 9b. In addition to the outer layer of alumina, an inner layer of alumina composed fine grains is formed after exposure in Ar with 20 vol.% O_2 at 1100°C for 50 h; see Fig. 13d. This layer is formed by the inward diffusion of oxygen through the outer layer of alumina. A very small amount of needle like oxides can be observed in between the outer and inner alumina layer, which is composed of Al_2O_3 - SiO_2 according to the composition analysis and elemental mapping; see Fig. 13c and 13e.

3.6.3. Oxidation kinetics after encapsulation

The mass change during exposure of the $\text{Mo}(\text{Al}_{0.40}\text{Si}_{0.60})_2$ particles to Ar with 20 vol.% O_2 at 1100°C recorded with TGA is shown in Fig. 14. An instant weight gain occurred after switching the gas composition to Ar with 20 vol.% O_2 , followed by a gradual weight loss. Note that the mass change amplitude caused by only switching of the gas composition is neglectable; see insert a of Fig. 14. Assuming that the weight gain amplitude is due to the selective oxidation of all the remaining Al in the core of the particles according to Eq. (1), then the weight gain can be calculated. This mass change is close to the observed mass gain amplitude of particle encapsulated in $p\text{O}_2$ of 5×10^{-10} atm. as indicated in Fig. 14. The

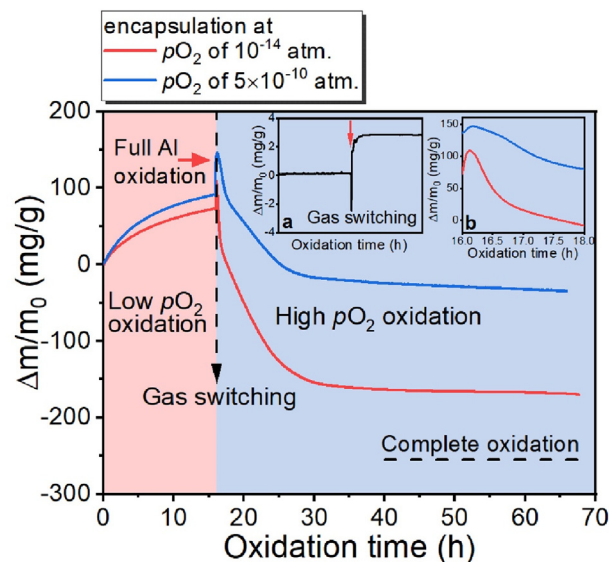


Fig. 14. Mass change of $\text{Mo}(\text{Al}_{0.40}\text{Si}_{0.60})_2$ particle during isothermal exposure at 1100°C . First to low oxygen partial pressure (i.e., $p\text{O}_2$ of 10^{-14} atm. and $p\text{O}_2$ of 5×10^{-10} atm., respectively) for 16 h. Subsequently, exposure to high oxygen partial pressure (i.e., Ar with 20 vol.% O_2) for 50 h. The insert (a) shows the mass change amplitude caused by switching the gas composition and insert (b) shows the initial oxidation upon gas switching. The dash line corresponds with the mass change of complete oxidation, i.e., when all $\text{Mo}(\text{Al}_{0.40}\text{Si}_{0.60})_2$ is oxidized into Al_2O_3 , SiO_2 and volatile MoO_3 .

subsequent gradual weight loss is due to the formation of volatile MoO_3 ; see the Supplementary Material 1.4 for detailed characterization. The formation of MoO_3 is likely due to particles that were not fully sealed by an alumina shell. Particles encapsulated in the $p\text{O}_2$ of 5×10^{-10} atm. exhibit slower mass loss after gas switching than those encapsulated in the $p\text{O}_2$ of 10^{-14} atm., indicating a better protection provided by the encapsulation in the $p\text{O}_2$ of 5×10^{-10} atm.; see insert b of Fig. 14. After about 15 h of exposure to high $p\text{O}_2$ of 0.2 atm. the mass change ceases, suggesting that the remaining particles will be preserved after long-time exposure to high temperature and high oxygen partial pressure. The particles encapsulated with a $p\text{O}_2$ of 10^{-14} atm. exhibit larger weight loss than those encapsulated with a $p\text{O}_2$ of 5×10^{-10} atm. The MoO_3 will act as a catalyst to promote the reaction between silica and alumina to form mullite ($3\text{Al}_2\text{O}_3 \cdot 2\text{SiO}_2$) and lowers the mullitization temperature [49,50], which explains the presence of mullite on the particles after exposure to Ar with 20 vol.% O_2 at 1100°C . Note that mullite is also capable to preserve the MoSi_2 core, although the diffusion coefficient of oxygen D in mullite ($D_0^{\text{lattice}} \sim 10^{-21} \text{m}^2/\text{s}$ and $D_0^{\text{gb}} \sim 10^{-17} \text{m}^2/\text{s}$ at 1100°C [51]) is higher than α - Al_2O_3 ($D_0^{\text{lattice}} \sim 10^{-26} \text{m}^2 \cdot \text{s}^{-1}$ and $D_0^{\text{gb}} \sim 10^{-19} \text{m}^2 \cdot \text{s}^{-1}$ at 1100°C). For comparison the oxygen diffusion coefficients of ZrO_2 and amorphous SiO_2 are $D_0^{\text{lattice}} \sim 10^{-11} \text{m}^2/\text{s}$ [15,52] and $D_{\text{O}_2} \sim 10^{-12} \text{m}^2/\text{s}$ [53], respectively.

Comparing the mass change behaviour of particles during exposure to Ar with 20 vol.% O_2 at 1100°C , after the pre-oxidation with $p\text{O}_2$ of 10^{-14} atm. and 5×10^{-10} atm. for 16 h, respectively, then a large difference in weight loss is observed; see Fig. 14. The weight loss, with respect to the value when the $\text{Mo}(\text{Al}_x\text{Si}_{1-x})_2$ particles are completely oxidized into Al_2O_3 , SiO_2 and MoO_3 , is about 86 % and 30 % for the particles after pre-oxidation with $p\text{O}_2$ of 10^{-14} atm. and 5×10^{-10} atm. for 16 h, respectively.

4. Conclusions

Encapsulation of $\text{Mo}(\text{Al}_x\text{Si}_{1-x})_2$ healing particles is designed in terms of alumina shell thickness, particle size and fraction Al dis-

solved. The conditions for the selective oxidation of Al to form a dense α -Al₂O₃ shell are determined based on thermodynamic and kinetic data.

Encapsulation with alumina of these sacrificial particles envisioned for self-healing yttria partially stabilized zirconia (YPSZ) thermal barrier coatings (TBCs) has been realized by selective oxidation of Al in Mo(Al_xSi_{1-x})₂ particles with x between 0.35 and 0.65 and an on average size of about 30 μ m. By replacing Si by Al in MoSi₂ still a strong crack damage healing ability is maintained (relative volume expansion $\geq 40\%$).

A closed shell of exclusively α -Al₂O₃ with thickness of about 0.8 μ m was formed after oxidation in a low oxygen partial pressure gas ambient of 10⁻¹⁴ atm. at 1100 °C for 16 h, whereby the formation of volatile molybdenum oxide species was mitigated. A two-layered structure, comprising of an equiaxed layer consists of fine grains and a thin columnar layer underneath, was observed in the α -Al₂O₃ scale which is ascribed to a counter-diffusion mechanism.

Increasing the oxygen partial pressure to 5 $\times 10^{-10}$ atm. still results in a shell of exclusively α -Al₂O₃ when oxidizing the Mo(Al_xSi_{1-x})₂ particles at 1100 °C for 16 h, but with a larger thickness of about 1.3 μ m. This higher oxygen partial pressure promotes the grain growth in both equiaxed and columnar layer and results in a dense α -Al₂O₃ scale.

The conversion from Al to Al₂O₃ does not increase with increasing the Al content of the original Mo(Al_xSi_{1-x})₂ particles. The growth of the alumina oxide shell by selective oxidation is captured with a 3-D diffusion-Jander (D3) reaction model. The conversion from Al to Al₂O₃ is practically independent of the Al content of the original Mo(Al_xSi_{1-x})₂ particles. The activation energy required for oxidation of the Mo(Al_xSi_{1-x})₂ particles with p_{O_2} of 10⁻¹⁴ atm. and 5 $\times 10^{-10}$ atm. equals to 84 \pm 11 kJ/mol and 184 \pm 22 kJ/mol, respectively, which is much lower than for the oxidation of alumina forming alloys with a flat surface (about 250 kJ/mol).

The Mo(Al_{0.4}Si_{0.6})₂ particles encapsulated by selective oxidation of Al with a p_{O_2} of 5 $\times 10^{-10}$ atm. at 1100 °C for 16 h are the most promising to prevent premature full oxidation in a self-healing thermal barrier coating system. After exposure to Ar with 20 vol. % O₂ at 1100 °C for 50 h, a core of pure MoSi₂ with a rim of Mo₅Si₃ is enveloped by a robust oxide shell of α -Al₂O₃. This encapsulation provides MoSi₂ particles with 86 % less weight loss upon oxidation preserving the healing capacity of the particles.

CRedit authorship contribution statement

Zhaoying Ding: Investigation, Formal analysis, Visualization, Writing – original draft. **Johannes C. Brouwer:** Validation, Formal analysis, Writing – review & editing. **Cees Kwakernaak:** Validation, Writing – review & editing. **Jia-Ning Zhu:** Validation, Writing – review & editing. **Vera Popovich:** Supervision, Resources, Writing – review & editing. **Marcel J.M. Hermans:** Supervision, Resources, Writing – review & editing. **Willem G. Sloof:** Conceptualization, Supervision, Resources, Project administration, Writing – review & editing.

Data availability

Data will be made available on request.

Declaration of Competing Interest

The authors declare that they have no known competing financial interests or personal relationships that could have appeared to influence the work reported in this paper.

Acknowledgements

This project has received funding from European Union Seventh Framework Programme (FP7/2007–2013) under grant agreement No. 309849, SAMBA. China Scholarship Council is acknowledged by Zhaoying Ding for their support (Grant No. 201806120145). The authors thank Ing. R.W.A. Hendrikx for the XRD analysis.

Data availability

Data will be made available on request.

Appendix A. Supplementary material

Supplementary data to this article can be found online at <https://doi.org/10.1016/j.matdes.2022.111577>.

References

- [1] N.P. Padture, M. Gell, E.H. Jordan, Thermal barrier coatings for gas-turbine engine applications, *Science* 296 (5566) (2002) 280–284, <https://doi.org/10.1126/science.1068609>.
- [2] X.Q. Cao, R. Vassen, D. Stoeber, Ceramic materials for thermal barrier coatings, *J. Eur. Ceram. Soc.* 24 (1) (2004) 1–10, [https://doi.org/10.1016/S0955-2219\(03\)00129-8](https://doi.org/10.1016/S0955-2219(03)00129-8).
- [3] D.R. Clarke, S.R. Phillpot, Thermal barrier coating materials, *Mater. Today* 8 (6) (2005) 22–29, [https://doi.org/10.1016/S1369-7021\(05\)70934-2](https://doi.org/10.1016/S1369-7021(05)70934-2).
- [4] Z. Derelioglu, A.L. Carabat, G.M. Song, S. van der Zwaag, W.G. Sloof, On the use of B-alloyed MoSi₂ particles as crack healing agents in yttria stabilized zirconia thermal barrier coatings, *J. Eur. Ceram. Soc.* 35 (16) (2015) 4507–4511, <https://doi.org/10.1016/j.jeurceramsoc.2015.08.035>.
- [5] L.B. Chen, Yttria-stabilized zirconia thermal barrier coatings—a review, *Surf. Rev. Lett.* 13 (2006) 535–544, <https://doi.org/10.1142/S0218625X060008670>.
- [6] A. Rabiei, A.G. Evans, Failure mechanisms associated with the thermally grown oxide in plasma-sprayed thermal barrier coatings, *Acta Mater.* 48 (2000) 3963–3976, [https://doi.org/10.1016/S1359-6454\(00\)00171-3](https://doi.org/10.1016/S1359-6454(00)00171-3).
- [7] Y. Chen, X. Zhang, S. van der Zwaag, W.G. Sloof, P. Xiao, Damage evolution in a self-healing air plasma sprayed thermal barrier coating containing self-shielding MoSi₂ particles, *J. Am. Ceram. Soc.* 102 (8) (2019) 4899–4910, <https://doi.org/10.1111/jace.16313>.
- [8] J. Krishnasamy, S.A. Ponnusami, S. Turteltaub, S. van der Zwaag, Modelling the fracture behaviour of thermal barrier coatings containing healing particles, *Mater. Des.* 157 (2018) 75–86, <https://doi.org/10.1016/j.matdes.2018.07.026>.
- [9] S.A. Ponnusami, J. Krishnasamy, S. Turteltaub, S. van der Zwaag, A cohesive-zone crack healing model for self-healing materials, *Int. J. Solids Struct.* 134 (2018) 249–263, <https://doi.org/10.1016/j.ijsolstr.2017.11.004>.
- [10] T.S. Hille, T.J. Nijdam, A.S.J. Suiker, S. Turteltaub, W.G. Sloof, Damage growth triggered by interface irregularities in thermal barrier coatings, *Acta Mater.* 57 (9) (2009) 2624–2630, <https://doi.org/10.1016/j.actamat.2009.01.022>.
- [11] A. Kumthekar, S.A. Ponnusami, S. van der Zwaag, S. Turteltaub, Uncertainty quantification of the lifetime of self-healing thermal barrier coatings based on surrogate modelling of thermal cyclic fracture and healing, *Mater. Des.* 221 (2022), <https://doi.org/10.1016/j.matdes.2022.110973>.
- [12] A.G. Evans, D.R. Mumm, J.W. Hutchinson, G.H. Meier, F.S. Pettit, Mechanisms controlling the durability of thermal barrier coatings, *Prog. Mater. Sci.* 46 (2001) 505–553, [https://doi.org/10.1016/S0079-6425\(00\)00020-7](https://doi.org/10.1016/S0079-6425(00)00020-7).
- [13] J. Aktaa, K. Sfar, D. Munz, Assessment of TBC systems failure mechanisms using a fracture mechanics approach, *Acta Mater.* 53 (16) (2005) 4399–4413, <https://doi.org/10.1016/j.actamat.2005.06.003>.
- [14] J. Krishnasamy, S.A. Ponnusami, S. Turteltaub, S. van der Zwaag, Thermal cyclic behavior and lifetime prediction of self-healing thermal barrier coatings, *Int. J. Solids Struct.* 222–223 (2021), <https://doi.org/10.1016/j.ijsolstr.2021.03.021>.
- [15] F. Nozahic, C. Estournès, A.L. Carabat, W.G. Sloof, S. van der Zwaag, D. Monceau, Self-healing thermal barrier coating systems fabricated by spark plasma sintering, *Mater. Des.* 143 (2018) 204–213, <https://doi.org/10.1016/j.matdes.2018.02.001>.
- [16] D. Koch, D.E. Mack, R. Vaßen, Degradation and lifetime of self-healing thermal barrier coatings containing MoSi₂ as self-healing particles in thermo-cycling testing, *Surf. Coat. Technol.* 437 (2022), <https://doi.org/10.1016/j.surfcoat.2022.128353>.
- [17] F. Nozahic, A.L. Carabat, W. Mao, D. Monceau, C. Estournès, C. Kwakernaak, S. van der Zwaag, W.G. Sloof, Kinetics of zircon formation in yttria partially stabilized zirconia as a result of oxidation of embedded molybdenum disilicide, *Acta Mater.* 174 (2019) 206–216, <https://doi.org/10.1016/j.actamat.2019.05.046>.
- [18] X.-P. Zhang, J.-H. Ouyang, Z.-G. Liu, Y.-J. Wang, Y.-M. Wang, Crack-healing behavior and strength recovery of hot-pressed TZ3Y20A–MoSi₂ ceramics, *Mater. Sci. Eng. A* 648 (2015) 299–304, <https://doi.org/10.1016/j.msea.2015.09.041>.

- [19] M. Yuan, L. Liu, J. Wang, Q. Hu, H. Zhang, S. Zhang, X. Zhou, Crack-healing behaviour of MoSi₂ dispersed Yb₂Si₂O₇ environmental barrier coatings, *Ceram. Int.* 48 (20) (2022) 29919–29928, <https://doi.org/10.1016/j.ceramint.2022.06.258>.
- [20] A.H. Heuer, T. Nakagawa, M.Z. Azar, D.B. Hovis, J.L. Smialek, B. Gleeson, N.D.M. Hine, H. Guhl, H.S. Lee, P. Tangney, W.M.C. Foulkes, M.W. Finnis, On the growth of Al₂O₃ scales, *Acta Mater.* 61 (18) (2013) 6670–6683, <https://doi.org/10.1016/j.actamat.2013.07.024>.
- [21] A.H. Heuer, Oxygen and aluminum diffusion in α -Al₂O₃: How much do we really understand?, *J. Eur. Ceram. Soc.* 28 (7) (2008) 1495–1507, <https://doi.org/10.1016/j.jeurceramsoc.2007.12.020>.
- [22] D.J. Young, *High temperature oxidation and corrosion of metals*, Elsevier, 2016.
- [23] A.L. Carabat, S. Zwaag, W.G. Sloof, T. Troczynski, Creating a protective shell for reactive MoSi₂ particles in high-temperature ceramics, *J. Am. Ceram. Soc.* 98 (8) (2015) 2609–2616, <https://doi.org/10.1111/jace.13625>.
- [24] A.L. Carabat, M.J. Meijerink, J.C. Brouwer, E.M. Kelder, J.R. van Ommen, S. van der Zwaag, W.G. Sloof, Protecting the MoSi₂ healing particles for thermal barrier coatings using a sol-gel produced Al₂O₃ coating, *J. Eur. Ceram. Soc.* 38 (7) (2018) 2728–2734, <https://doi.org/10.1016/j.jeurceramsoc.2018.02.002>.
- [25] T.J. Nijdam, L.P.H. Jeurgens, W.G. Sloof, Promoting exclusive α -Al₂O₃ growth upon high-temperature oxidation of NiCrAl alloys: experiment versus model predictions, *Acta Mater.* 53 (6) (2005) 1643–1653, <https://doi.org/10.1016/j.actamat.2004.12.014>.
- [26] T.J. Nijdam, L.P.H. Jeurgens, W.G. Sloof, Modelling the thermal oxidation of ternary alloys—compositional changes in the alloy and the development of oxide phases, *Acta Mater.* 51 (18) (2003) 5295–5307, [https://doi.org/10.1016/S1359-6454\(03\)00381-1](https://doi.org/10.1016/S1359-6454(03)00381-1).
- [27] M. Białaś, Finite element analysis of stress distribution in thermal barrier coatings, *Surf. Coat. Technol.* 202 (24) (2008) 6002–6010, <https://doi.org/10.1016/j.surfcoat.2008.06.178>.
- [28] M. Ranjbar-Far, J. Absi, S. Shahidi, G. Mariaux, Impact of the non-homogenous temperature distribution and the coatings process modeling on the thermal barrier coatings system, *Mater. Des.* 32 (2) (2011) 728–735, <https://doi.org/10.1016/j.matdes.2010.07.034>.
- [29] L. Ingemarsson, K. Hellström, S. Canovic, T. Jonsson, M. Halvarsson, L.G. Johansson, J.E. Svensson, Oxidation behavior of a Mo(Si, Al)₂ composite at 900–1600 °C in dry air, *J. Mater. Sci.* 48 (4) (2012) 1511–1523, <https://doi.org/10.1007/s10853-012-6906-0>.
- [30] A. Khawam, D.R. Flanagan, Solid-state kinetic models: basics and mathematical fundamentals, *J. Phys. Chem. B* 110 (2006) 17315–17328, <https://doi.org/10.1021/jp062746a>.
- [31] C. Rozycki, M. Maciejewski, Method of the selection of the g(α) function based on the reduced-time plot, *Thermochim. Acta* 122 (1987) 339–364, [https://doi.org/10.1016/0040-6031\(87\)87052-1](https://doi.org/10.1016/0040-6031(87)87052-1).
- [32] W.B. Gong, C.K. Sha, D.Q. Sun, W.Q. Wang, Microstructures and thermal insulation capability of plasma-sprayed nanostructured ceria stabilized zirconia coatings, *Surf. Coat. Technol.* 201 (6) (2006) 3109–3115, <https://doi.org/10.1016/j.surfcoat.2006.06.041>.
- [33] M.R. Loghman-Estarki, M. Pourbafrany, R. Shoja Razavi, H. Edris, S.R. Bakhshi, M. Erfanmanesh, H. Jamali, S.N. Hosseini, M. Hajizadeh-Oghaz, Preparation of nanostructured YSZ granules by the spray drying method, *Ceram. Int.* 40(2) (2014) 3721–3729, <https://doi.org/10.1016/j.ceramint.2013.09.050>.
- [34] K. Prabhakaran, M.O. Beigh, J. Lakra, N.M. Gokhale, S.C. Sharma, Characteristics of 8 mol% yttria stabilized zirconia powder prepared by spray drying process, *J. Mater. Process. Technol.* 189 (1–3) (2007) 178–181, <https://doi.org/10.1016/j.jmatprotec.2007.01.019>.
- [35] A.A. Sharif, High-temperature oxidation of MoSi₂, *J. Mater. Sci.* 45 (4) (2010) 865–870, <https://doi.org/10.1007/s10853-009-4012-8>.
- [36] Z. Ding, J.C. Brouwer, C. Kwakernaak, M.J.M. Hermans, V. Popovich, W.J. Quadackers, W.G. Sloof, Selective oxidation of aluminium in Mo(Al, Si)₂, *Corros. Sci.* 211 (2023), <https://doi.org/10.1016/j.corsci.2022.110884> 110844.
- [37] T. Maruyama, K. Yanagihara, High temperature oxidation and peeling of Mo(Si, Al)₂, *Mater. Sci. Eng. A* 230–240 (1997) 828–841, [https://doi.org/10.1016/S0921-5093\(97\)00673-4](https://doi.org/10.1016/S0921-5093(97)00673-4).
- [38] D.J. Tallman, B. Anasori, M.W. Barsoum, A critical review of the oxidation of Ti₂AlC, Ti₃AlC₂ and Cr₂AlC in Air, *Mater. Res. Lett.* 1 (3) (2013) 115–125, <https://doi.org/10.1080/21663831.2013.806364>.
- [39] R.H. Doremus, Oxidation of alloys containing aluminum and diffusion in Al₂O₃, *J. Appl. Phys.* 95 (6) (2004) 3217–3222, <https://doi.org/10.1063/1.1649454>.
- [40] L. Boatema, J.C. Brouwer, S. van der Zwaag, W.G. Sloof, The effect of the TiC particle size on the preferred oxidation temperature for self-healing of oxide ceramic matrix materials, *J. Mater. Sci.* 53 (8) (2018) 5973–5986, <https://doi.org/10.1007/s10853-017-1973-x>.
- [41] J. Šesták, Rationale and fallacy of thermoanalytical kinetic patterns, *J. Therm. Anal. Calorim.* 110 (1) (2011) 5–16, <https://doi.org/10.1007/s10973-011-2089-1>.
- [42] A.H. Heuer, D.B. Hovis, J.L. Smialek, B. Gleeson, Alumina scale formation: a new perspective, *J. Am. Ceram. Soc.* 94 (2011), <https://doi.org/10.1111/j.1551-2916.2011.04573.x>.
- [43] V.K. Tolpygo, D.R. Clarke, Microstructural evidence for counter-diffusion of aluminum and oxygen during the growth of alumina scales, *Mater. at High Temp.* 20 (3) (2014) 261–271, <https://doi.org/10.1179/mht.2003.030>.
- [44] H.J. Yang, Y.T. Pei, J.T.M. De Hosson, Oxide-scale growth on Cr₂AlC ceramic and its consequence for self-healing, *Scr. Mater.* 69 (2) (2013) 203–206, <https://doi.org/10.1016/j.scriptamat.2013.04.013>.
- [45] J.A. Nychka, D.R. Clarke, Quantification of aluminum outward diffusion during oxidation of FeCrAl alloys, *Oxid. Met.* 63 (5–6) (2005) 325–352, <https://doi.org/10.1007/s11085-005-4391-4>.
- [46] P. Vomacka, O. Babushkin, R. Warren, Zirconia as a nucleating agent in a yttria-alumina-silica glass, *J. Eur. Ceram. Soc.* 15 (1995) 1111–1117, [https://doi.org/10.1016/0955-2219\(95\)00086-A](https://doi.org/10.1016/0955-2219(95)00086-A).
- [47] N. Sadiki, J.P. Coutures, C. Fillet, J.L. Dussossoy, Crystallization of lanthanum and yttrium aluminosilicate glasses, *J. Nucl. Mater.* 348 (1–2) (2006) 70–78, <https://doi.org/10.1016/j.jnucmat.2005.09.003>.
- [48] T. Ohashi, T. Harada, High-temperature oxidation of Fe-Cr-Al-Si alloys extruded into honeycomb structures, *Oxid. Met.* 46 (1996) 235–254, <https://doi.org/10.1007/BF01050798>.
- [49] L. Zhu, Y. Dong, S. Hampshire, S. Cerneaux, L. Winnubst, Waste-to-resource preparation of a porous ceramic membrane support featuring elongated mullite whiskers with enhanced porosity and permeance, *J. Eur. Ceram. Soc.* 35 (2) (2015) 711–721, <https://doi.org/10.1016/j.jeurceramsoc.2014.09.016>.
- [50] Z. Zhu, Z. Wei, J. Shen, L. Zhu, L. Xu, Y. Zhang, S. Wang, T. Liu, Fabrication and catalytic growth mechanism of mullite ceramic whiskers using molybdenum oxide as catalyst, *Ceram. Int.* 43 (2) (2017) 2871–2875, <https://doi.org/10.1016/j.ceramint.2016.11.035>.
- [51] P. Fielitz, G. Borchardt, Oxygen grain-boundary diffusion in polycrystalline mullite ceramics, *J. Am. Ceram. Soc.* 87 (12) (2004) 2232–2236, <https://doi.org/10.1111/j.1151-2916.2004.tb07497.x>.
- [52] A. Madeysk, W.W. Smeltzer, Oxygen diffusion in monoclinic zirconia, *Mater. Res. Bull.* 3 (1968) 369–376, [https://doi.org/10.1016/0025-5408\(68\)90008-1](https://doi.org/10.1016/0025-5408(68)90008-1).
- [53] M.A. Lamkin, F.L. Riley, R.J. Fordham, Oxygen mobility in silicon dioxide and silicate glasses: a review, *J. Eur. Ceram. Soc.* 10 (1992) 347–367, [https://doi.org/10.1016/0955-2219\(92\)90010-B](https://doi.org/10.1016/0955-2219(92)90010-B).